Technical report on spin polarizabilities of the proton by measurement of Compton double-polarization observables

D. Paudyal* and G. M. Huber
University of Regina, Regina, Saskatchewan S4S 0A2, Canada

P. P. Martel
Mount Allison University, Sackville, New Brunswick E4L 1E6, Canada and
Institut für Kernphysik, University of Mainz, 55128 Mainz, Germany

D. Hornidge
Mount Allison University, Sackville, New Brunswick E4L 1E6, Canada
(Dated: August 3, 2019)

This report outlines technical support of the manuscript on "Spin polarizabilities of the proton via measurement of Compton double-polarization observables" that was submitted to the A2 collaboration for internal review. It also presents π^0 photoproduction Σ_{2z} asymmetry results from polarized Compton scattering performed at the Mainz Microtron. The experiments were run during two periods, May 2014 and June/July 2015, using a circularly polarized photon beam incident on a longitudinally polarized, frozen spin butanol target. In addition, this report summarizes various corrections that are vital for Σ_{2z} Compton scattering asymmetry studies including carbon and helium background subtractions, and target polarization studies.

I. INTRODUCTION

Proton Compton scattering, $\gamma p \to \gamma p$, is only one of the many interactions that can occur when photons hit a nuclear target. Although Compton scattering seems to have a simple final state, it is very important to correctly identify the individual particles detected in the Crystal Ball (CB) and Two-Arm Photon Spectrometer (TAPS) detector systems. The background from other competing reactions has to be identified and suppressed with several analyses of the reaction kinematics. The biggest challenge is to properly understand the π^0 photoproduction background because its cross section is about one hundred times larger than that of Compton scattering. Therefore, exclusive π^0 photoproduction is not only a significant source of "physics background" to Compton scattering experiments, but also a useful reaction for systematic tests of experimental systems and methodology of the analysis.

This report provides an overview of the π^0 photoproduction asymmetry analysis and checks on various corrections applied to the Compton Σ_{2z} asymmetry studies. In addition, this report provides a cross-check on polarization correction factors, for the frozen spin target (FST), reported by the Bonn group due to an extra layer of ice on the outer nuclear magnetic resonance (NMR) coil apparent in some of the data runs taken from May 2013 to September 2015 [1]. This was done by including the simulation of coherent π^0 production on ^{4}He in the π^0 asymmetry analysis (Sec. III C 3), subtracting helium data taken by the Bonn group in the π^0 asymmetry analysis (Sec. IV A), and from a helicity dependent cross section analysis (Sec. V).

II. π^0 Σ_{2z} ASYMMETRY

The π^0 photoproduction asymmetry Σ_{2z} can be expressed in terms of the polarized cross section with a flip in the polarization direction as:

$$\Sigma_{2z} = \frac{1}{P^{\gamma}_{circ} \cdot P^{t}_{z}} \left[\frac{(\sigma^{R}_{+z} + \sigma^{L}_{-z}) - (\sigma^{L}_{+z} + \sigma^{R}_{-z})}{(\sigma^{R}_{+z} + \sigma^{L}_{-z}) + (\sigma^{L}_{+z} + \sigma^{R}_{-z})} \right], \quad (1)$$

where $\sigma^{R}_{\pm z}$ and $\sigma^{L}_{\pm z}$ represent the cross section for right- and left-handed helicity states of the beam with the target polarized in the $\pm z$ direction, and P^{γ}_{circ} and P^{t}_{z} are the degrees of the photon beam circular polarization and longitudinal target polarization, respectively. This can be simply visualized from the four beam-target orientations as shown in Figs. 1a–1d.

The benefit of calculating an asymmetry is that the absolute normalizations (target density, beam flux, tagging and detection efficiencies) that relate the cross section to the number of events, N, cancel in the ratio. Therefore, the asymmetry formula in terms of count rate can be written as follows:

$$\Sigma_{2z} = \frac{1}{P^{\gamma}_{circ} \cdot P^{t}_{z}} \left[\frac{(N^{R}_{+z} + N^{L}_{-z}) - (N^{L}_{+z} + N^{R}_{-z})}{(N^{R}_{+z} + N^{L}_{-z}) + (N^{L}_{+z} + N^{R}_{-z})} \right], \quad (2)$$

where $N^{R}_{\pm z}$ and $N^{L}_{\pm z}$ are the normalized yields for right-

* paudyald@uregina.ca

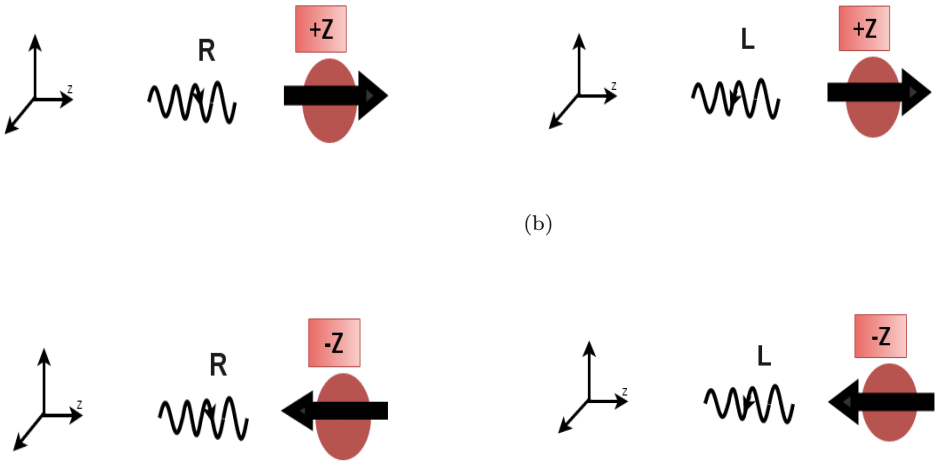

(a) (b)

(c) (d)

FIG. 1: Different orientations for π^0 photoproduction with a circularly polarized photon beam on a longitudinally polarized target. (a), (b) show the right- and left-handed helicity state of the beam, respectively, with target polarization in the $+z$ direction (σ^R_{+z}, σ^L_{+z}). (c) and (d) show the right- and left-handed helicity state of the beam, respectively, with target polarization in the $-z$ direction (σ^R_{-z}, σ^L_{-z}).

and left-handed helicity states of the beam, respectively, with the target polarized in the $\pm z$ direction.

III. BASIC ANALYSIS STEPS

In this section, the data analysis steps for the $\gamma p \to \pi^0 p$ reaction channel, identification and reconstruction of particles (photons and protons) directly observed in the CB-TAPS detector system, the reconstruction of the π^0 from its decay, $\pi^0 \to \gamma\gamma$, and the various kinematic cuts applied are presented.

A. Particle Identification

To identify the particles of interest for the reaction channel, $\gamma p \to \pi^0 p$, with the π^0 decaying into two photons ($\pi^0 \to \gamma\gamma$), individual particle tracks were identified. The experimental setup, combining the CB and TAPS detectors with additional detector elements for charged particle identification and tracking was identical to the one used for the results reported in Ref. [2]. The cylindrical Particle Identification Detector (PID) consists of 24 plastic scintillators parallel to the beam axis surrounded by Multi-Wire Proportional Chambers (MWPCs). They are mounted around the target cell. By matching a hit in the PID with a corresponding hit in the CB, it is possible to use the $\Delta E/E$ technique to identify the charged particle species. In this technique, an energy deposition in the PID coincident with an energy deposition in a cluster in the CB is used for the separation of charged pions, electrons, and protons. For the lighter particles, like electrons and pions, the energy deposition is roughly $1-2$ MeV. However, heavier particles like the proton deposit energy inversely proportional to their total energy, with slower protons depositing a higher fraction of their total energy. A two-dimensional histogram of the energy loss, ΔE, measured in the PID, and the energy, E, measured in the CB, results in two distinct bands associated with different particle species. In addition, the MWPCs were used to identify a charged particle track. In the case of TAPS, the veto detector tiles in front of each BaF_2 crystals are used. A cluster is identified as a charged particle if the veto tile in front of the cluster's central crystal is hit, and a cut placed on the cluster size separates the photons and neutrons (details can be found in Ref. [2]). While the detection of the proton can assist in reducing background, the efficiency of this detection is rather low, and it is therefore not required since the reconstruction of the π^0 fully constrains the system.

B. π^0 Reconstruction

The analysis of the reaction channel $\gamma p \to \pi^0 p$ requires events with exactly two time-correlated neutral particles in CB-TAPS that are further time-correlated with a hit in the tagger. This is due to the fact that some photons from the beam pass through without interacting, while many others are lost due to collimation of the beam. The events in the tagger that are in timing coincidence with the photons interacting with the target are called "prompt" events while those without any timing coincidences are "random" events. These uncorrelated events, which are normally referred to as background events, are numerous and hence need to be subtracted during the analysis. Fig. 2 shows the

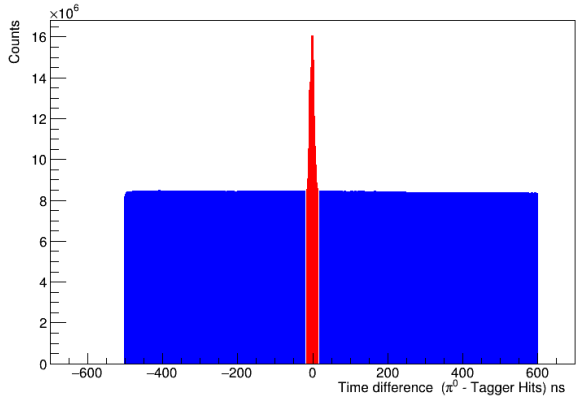

FIG. 2: Difference between the tagger and π^0 times; the prompt and random windows are shown in red and blue, respectively.

prompt and random timing windows for event hits in the tagger, which are in timing coincidence with the reconstructed π^0. The prompt electrons, which occur for hits in that detector element which correspond to photons that interacted with the target, have a peak around 0 ns (shown in red) whereas the random electrons form the flat distribution that extends to either side of the prompt peak (blue background). A timing coincidence window of 30 ns is used to identify prompt electrons. Since the prompt peak sits on top of this flat background associated with random electrons, a random coincidence subtraction was performed based on the weighted events of the random window on either side of the prompt peak.

The energy and momentum information of the two decay photons is used to reconstruct π^0 mesons. The invariant mass of the π^0 is defined as

$$M_{\gamma\gamma} = \sqrt{E_{\gamma\gamma}^2 - \vec{p}_{\gamma\gamma}^{\,2}} = \sqrt{\left(E_{\gamma_1} + E_{\gamma_2}\right)^2 - \left(\vec{p}_{\gamma_1} + \vec{p}_{\gamma_2}\right)^2}, \quad (3)$$

where E_{γ_1}, E_{γ_2}, $\vec{p}_{\gamma_1}$ and $\vec{p}_{\gamma_2}$ are the energy and the momentum vectors of the two photons, respectively. The π^0 reconstruction is performed to identify particles belonging only to its decay. A photon pair resulting from a π^0 decay should have an invariant mass of 134.98 MeV. An invariant mass cut, with a width $w_{\pi^0} = \pm 17.5$ MeV, was applied, as shown in Fig. 3.

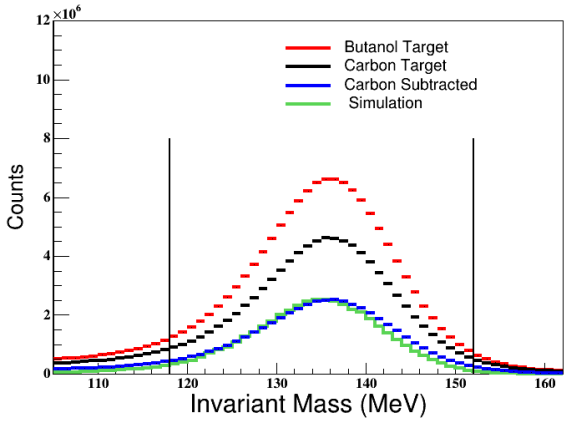

FIG. 3: An example invariant mass distribution (red: butanol target, black: carbon target, blue: carbon subtracted and green: simulation) for reconstructed π^0 photoproduction events at tagged photon energy, $E_\gamma = 285 - 305$ MeV. The two black vertical lines show a cut applied on the invariant mass.

C. Carbon Background and Checks on Scaling Factors

In this section, additional corrections and checks for consistency not covered in D. Paudyal's thesis [2] are described. It should be pointed out that the four-fold method of subtraction (see Sec. II) was applied in this data analysis compared to the two-fold method as carried out in Ref. [2].

1. *Base Carbon Scaling Factor*

The Σ_{2z} asymmetry experimental runs were broken down into two main parallel and anti-parallel data sets as well as subsets for positive and negative butanol target polarization runs for both the 2014 and 2015 beamtimes. In addition to the butanol target, separate dedicated data sets were taken with the carbon target before or after their respective butanol beamtimes. This was required to remove any contribution from the non-hydrogen elements in the butanol target. While the

target is not a pure proton target, the unpolarized background from heavier nuclei such as carbon and oxygen present in the butanol target can be partly removed by kinematic studies. These carbon data were analyzed using the same physics classes within the A2GoAT framework [3] as the butanol data. Subtracting out the carbon contribution to the missing mass spectra, a carbon scaling factor is needed to scale the carbon target data to each of the subsets of polarized butanol target data.

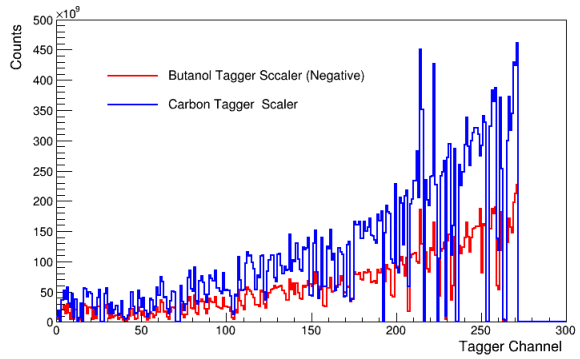

FIG. 4: An example tagger scaler distribution for negatively polarized butanol target and carbon target from the 2014 beamtime.

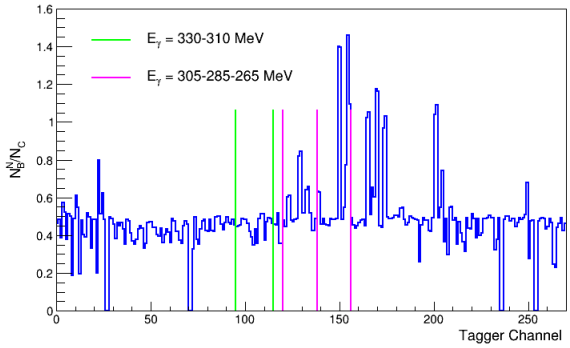

FIG. 5: Ratio of negatively polarized butanol target to carbon tagger scalers from the 2014 beamtime. The vertical lines show the tagged energy range of interest corresponding to tagger channels. The fluctuations represent missing tagger channels not the statistical fluctuations.

The ratio of the overall butanol target integrated luminosity to the overall carbon target integrated luminosity was determined and termed the "base scaling factor". This was done by adding live-time corrected individual tagger scaler histograms for the entire data set (one for positive, one for negative target polarization, and one for the carbon background target) and dividing the butanol by the carbon data subset. The base scaling factor is different for different subsets, as well as for different regions of the tagger. An example distribution of negatively polarized butanol (blue) and carbon target total histograms (red) from the 2014 beamtime are shown in Fig. 4 and the ratio between them for each tagger channel is shown in Fig. 5. Similarly, the positively polarized butanol (blue) and carbon target total histograms (red) and the ratio between them corresponding to each tagger channel are shown in Appendix D (Fig. 51a and Fig. 51b).

2. *Additional Carbon Scaling Factor*

The base carbon scaling factor was obtained from a ratio of tagger scalers. However, this was insufficient to account for the nuclear π^0 photoproduction background due to additional nuclear effects and hence the missing mass ratio method was used to find the extra correction needed to properly scale the carbon runs. For this, missing mass spectra for the carbon target were scaled by the base scaling factor and then the missing mass spectra obtained with the butanol target were divided by the missing mass spectra obtained with the carbon target for the π^0 photoproduction channel. A combination of a Gaussian distribution and a constant was fitted to the resulting spectra. The magnitude of the constant fitting parameter (Fig. 6) was used as an extra scaling factor. This was done separately for all four beam-target orientations and eighteen angular bins (see Appendix D), and an example plot is shown in Fig. 7. The source of the systematic error arose mainly from the choice of fitting range. This range was varied from ± 40 MeV from the mean position of the spectrum and the average deviation of the π^0 photoproduction was used to determine the systematic uncertainty [2].

3. *Determination of Helium Scaling Factor*

To study the coherent background from the liquid ^{4}He bath surrounding the target, a Monte Carlo (MC) simulation of $\gamma\ ^4\text{He} \rightarrow ^4\text{He}\ \pi^0$ was utilized. First, a home built event generator took care of the proper kinematics, the output files were then passed through a Geant4 simulation, and finally they were analyzed using the same framework as that for the experimental data. In addition, the MC simulation of $\gamma p \rightarrow \pi^0 p$ was also performed. The missing mass distributions from these two simulations were scaled such that their sum matched the overall carbon subtracted missing mass distributions. This ^{4}He scaling factor was then used at each π^0 angle to remove this background, after which the asymmetry

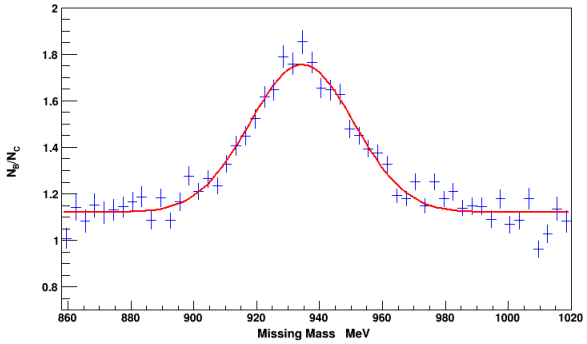

FIG. 6: An example spectrum of the ratio of missing proton mass for butanol and carbon targets in the energy range $E_\gamma = 285 - 305$ MeV at photon angle $\theta = 110 - 120°$ for the P0C0 (see Appendix C for nomenclature details) dataset. The red line is the combined fit of a Gaussian distribution plus a constant term. The fit parameter of the constant defines the extra carbon scaling factor.

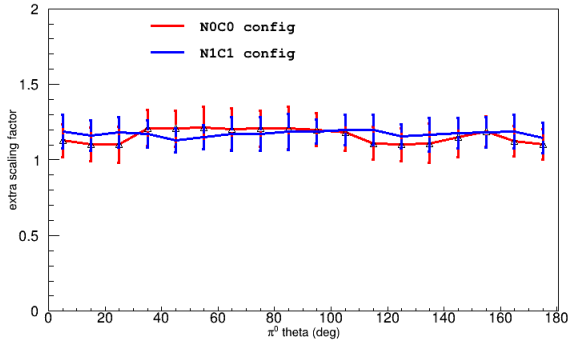

FIG. 7: Example extra carbon scaling factors for negatively polarized target orientation from the 2014 beamtime. See Appendix C for nomenclature details.

was determined. An example of the sum of the two MC simulations of (coherent) π^0 photoproduction off of the proton or ^{4}He along with the experimental data distribution is shown in Fig. 8.

D. Missing Mass for π^0 Photoproduction Events

The following section details missing mass studies for π^0 photoproduction events from both the 2014 and 2015 beamtimes. The analysis of missing mass is one of the most powerful steps to address background not eliminated by the invariant mass analysis (see Sec. III A). The data analysis was carried out separately for four beam-target configurations, and each of the configurations was divided into eighteen polar-angle bins of 10° each. See Ref. [2] for complete details on further data selection criteria and various kinematic cuts on the $\gamma p \to \pi^0 p$ reaction channel.

As mentioned above, the frozen spin target contains carbon and oxygen in the butanol plus the liquid helium as a cryogen, and they contribute a major source of background in the experiment. Therefore, a separate data run was taken with a carbon target by inserting it into the same cryostat to account for this. It was very important to insert the carbon target into the same target cell because the subtraction removes any contribution from the windows, and/or shells of the cryostat material. Although this was done, the procedure is not perfect and the carbon subtraction has under-performed in several experiments [4, 5].

Over the past few years, there have been discussions within the collaboration on the requirement of having separate helium target data and including it in the analysis to address the background from the ^{4}He refrigeration material. For this analysis the simulation of coherent π^0 production on ^{4}He is matched to the data via a scaling factor (Sec. III C 3). To do this, MC simulation of events for π^0 photoproduction off of proton and off of a helium target were generated as discussed in Sec. III C 3, and the sum of the two contributions have been compared to distributions from the experimental data. Fig. 8 shows an example missing mass spectrum at $\theta_{\pi^0} = 50 - 60°$ for the N1C1 beam-target configuration from the 2015 beamtime (see Appendix C for nomenclature details). Overall there is good agreement between the experimental missing mass distribution and the sum of these two simulations, and therefore the simulated distributions using the extracted helium scale factor are used for comparison over all π^0 angles.

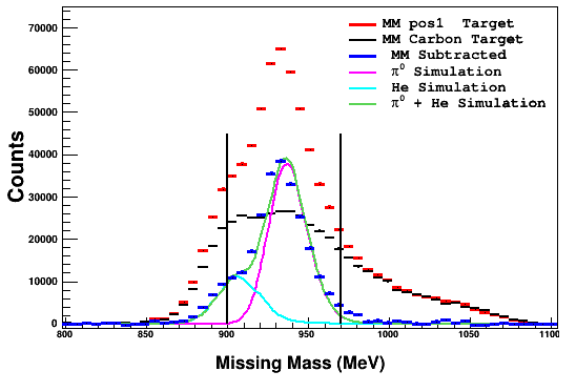

FIG. 8: Missing mass spectra at $\theta_{\pi^0} = 50 - 60°$ and $E_\gamma = 310 - 330$ MeV for the π^0 photoproduction channel from the 2015 beamtime. The two vertical lines represent the missing mass integration limit.

Furthermore, the missing mass spectra were studied over all θ_{π^0} angles and all four beam-target orientations for both the 2014 and 2015 beamtimes, the results are included in Appendix C (Figs. 43–50).

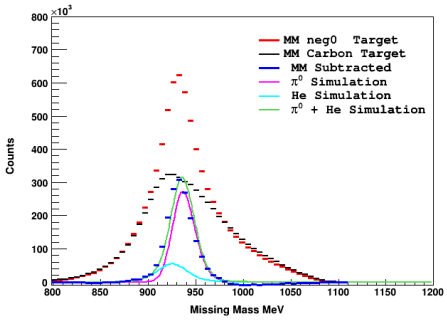

FIG. 9: Missing mass spectra over all θ_{π^0} angles at $E_\gamma = 285 - 305$ MeV for the π^0 photoproduction channel from the 2015 beamtime.

E. Target Polarization for 2014 Beamtime

A precise knowledge of target polarization is essential for the determination of π^0 and Compton Σ_{2z} asymmetries because these values enter as a normalization factor in the asymmetry formula. In their analysis of beamtimes neighboring the 2014 and 2015 Compton beamtimes, the Bonn group concluded that the values reported for the target polarization were incorrect [9]. To account for this, they determined target polarization correction factors of 1.4 and 1.15 for their 2014 and 2015 beamtimes, respectively. The target group reported an explanation of these polarization issues at the 2016 March Collaboration meeting [1], having found in their study that the possibility of an extra layer of ice on the NMR coil (Fig. 10) could dilute the measured polarization value for any data taken from May 2013 to September 2015. Table I shows both the reported target polarization and polarization values after applying these corrections determined by the Bonn group. Note that target polarization measurements are not possible during data taking because the polarizing magnet does not fit within the geometry of the CB detector. Moreover, the magnetic field strength and homogeneity of the holding coil is not sufficient for polarization measurements. Therefore, the maximum polarization, P_i^T, at the start of the data taking period and final polarization, P_f^T, at the end of the data taking period, for separate target polarization orientations are included. It should be pointed out that the polarization did not drop below 50% over the data taking period for either orientation, and thus repolarization of the target was not required.

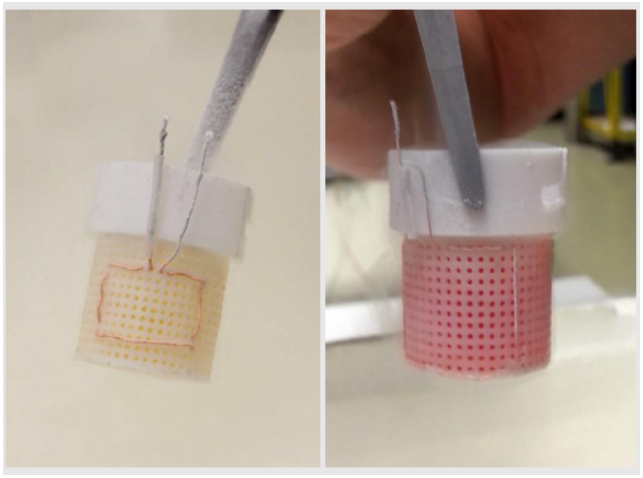

FIG. 10: Proton NMR coils for May 2014 (left) and for May 2015 (right) beamtimes [1, 7]

.

Start date	End date	P_i^T(%)	P_f^T(%)	P_i^{TC}(%)	P_f^{TC}(%)
02.05.2014	12.05.2014	63.6	58.7	89.0	82.2
13.05.2014	19.05.2014	-61.6	-53.7	-84.8	-75.2

TABLE I: Summary of target polarization at the start (P_i^T) and end (P_f^T) of the data taking periods, as determined by[7, 8] (third and fourth columns) and after correction by the suggested factor of 1.4 [9] (P_i^{TC} and P_f^{TC} in the fifth and sixth columns), for the 2014 beamtime.

F. Target Polarization for 2015 Beamtime

The target polarization measurements for the 2015 beamtime are shown in Table II [7]. The corrected target polarization values after applying corrections discussed in Sec. III E are as shown in the fifth and sixth columns of Table II.

Start date	End date	P_i^T(%)	P_f^T(%)	P_i^{TC}(%)	P_f^{TC}(%)
23.06.2015	02.07.2015	74.2	62.7	85.4	72.1
02.07.2015	11.07.2015	-65.2	-49.0	-74.8	-56.4

TABLE II: Summary of target polarization at the start (P_i^T) and end (P_f^T) of the data taking periods, as determined in Ref. [7] (third and fourth columns) and after correction by the suggested factor of 1.15 [9] (P_i^{TC} and P_f^{TC} in the fifth and sixth columns), for the 2015 beamtime.

IV. π^0 Σ_{2z} ASYMMETRY RESULTS

The π^0 photoproduction reaction, compared to Compton scattering, has a relatively background-free signal due to its large cross section and the CB-TAPS experimental set-up. However, it is important to apply various kinematic cuts and correct scaling factors, including those for subtracting the carbon data and the MC simulation of coherent production on helium (see Sec. V A). The π^0 photoproduction asymmetries as a function of π^0 angle from both the 2014 and 2015 beamtimes are shown in Fig. 11, along with both SAID [10] and MAID models [11]. The π^0 asymmetry results indicate that the extra correction factors are needed.

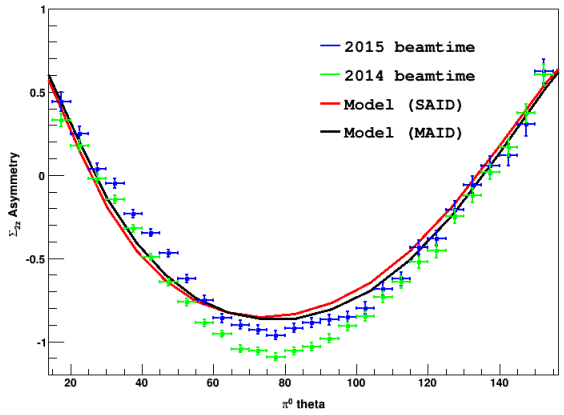

FIG. 11: π^0 asymmetry results without the extra target polarization correction factors at $E_\gamma = 285 - 305$ MeV.

Fig. 12 shows the π^0 asymmetry results including target polarization correction factors (1.26 ± 0.03 and 1.12 ± 0.02 for the 2014 and 2015 beamtimes, respectively). It should be noted that the 2014 factor of 1.26 and the factor of 1.4 reported by Bonn should match, due to the two beamtimes being back-to-back, implying that any ice on the NMR coil should be constant. On the other hand, the 2015 factor of 1.12 and the factor of 1.15 reported by Bonn do not need to match, as these beamtimes were separated with a target warm-up and cool-down. These factors were determined by minimizing the χ^2 per degree of freedom for both the 2014 and 2015 beamtimes. The average of the SAID and MAID models was also determined. It is clearly seen that the Σ_{2z} asymmetry results for the π^0 photoproduction events are in good agreement (within the statistical uncertainties) with both the SAID and MAID models after applying these extra correction factors at the given energy range. This agreement with the SAID and MAID models provides justification for the applied correction factors. This factor is cross checked from

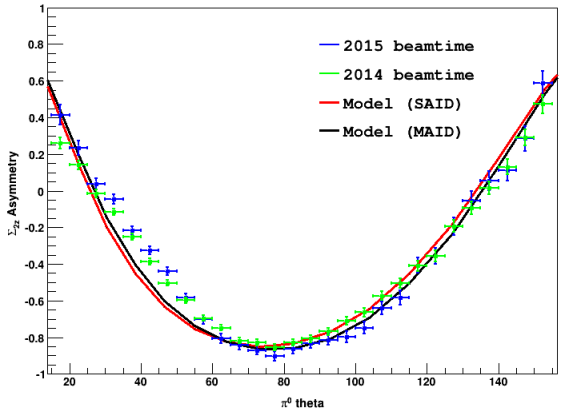

FIG. 12: π^0 asymmetry results with an extra target polarization factor (1.26 and 1.12 from the 2014 and 2015 beamtimes, respectively) applied at $E_\gamma = 285 - 305$ MeV.

polarized and unpolarized cross section studies and is presented in Sec. V.

A. Utilization of Helium Data from Sep 2015 G-E Beamtime

The Bonn group had suggested that the data taken in September 2015, where the cryostat was filled with helium with the carbon target in place, could perhaps be used for this analysis. Due to a number of differences between these beamtimes (MAMI energy, trigger selection, usage of Cherenkov detector), this is not practical for the complete subtraction of the non-hydrogen background in the FST. However, there were also a number of runs in September 2015 taken with either just helium in the cryostat or an entirely empty cryostat. From these, a small amount of data can be constructed for the helium bath by itself. If this helium-only data is scaled by the flux to match the 2014 Compton data and by the target density to match the helium bath in the FST, it can be used in addition to the standard carbon data to subtract out the background. An example of this for $E_\gamma = 270 - 290$ MeV and $\theta_{\pi^0}^{\rm cm} = 50 - 70^\circ$ is shown in Fig. 13. One can observe the slight bump at 900 MeV, where the subtraction is not sufficient, but otherwise matches very well. Integrating over all angles gives Fig. 14.

Using these carbon and helium subtracted missing masses, the π^0 E-asymmetry (Σ_{2z}) can be constructed for both the 2014 and 2015 beamtimes, where polarization correction factors of 1.4 and 1.25, respectively, were required to obtain reasonable agreement with SAID. The 2014 and 2015 results are shown in Fig. 15 and

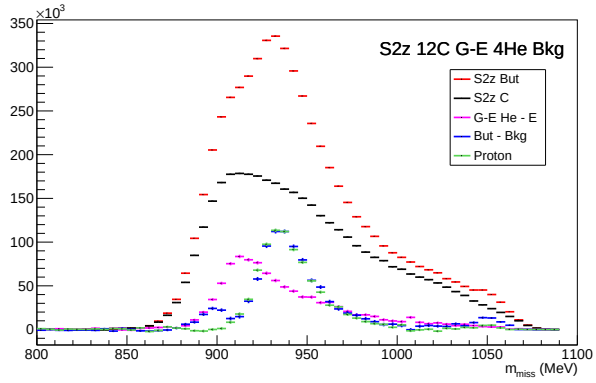

FIG. 13: π^0 missing mass for $E_\gamma = 270 - 290$ MeV and $\theta^{\rm cm}_{\pi^0} = 50 - 70°$.

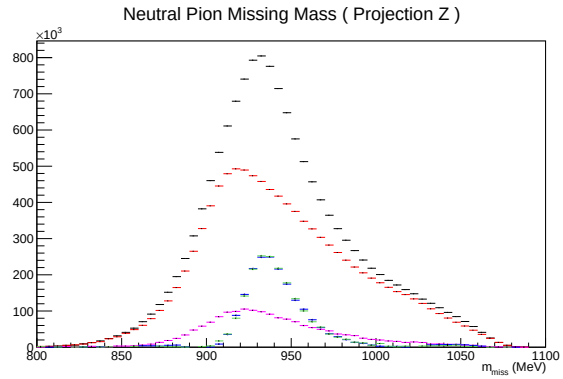

FIG. 14: π^0 missing mass for $E_\gamma = 270 - 290$ MeV over all angles.

Fig. 16, respectively.

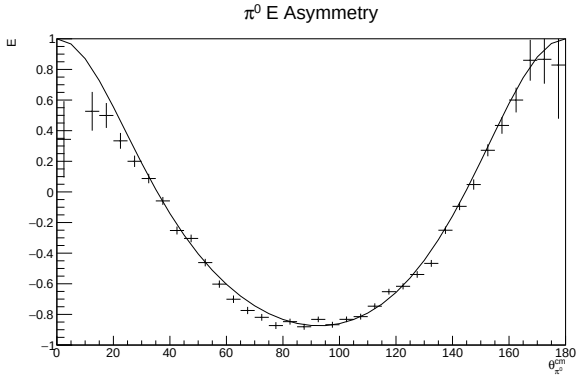

FIG. 15: π^0 E (Σ_{2z}) asymmetry for the 2014 beamtime, with a target polarization correction of 1.4. The curve is the CM12 solution from SAID [10].

This method results in the same polarization correction factor as the Bonn group for 2014, where the beam-

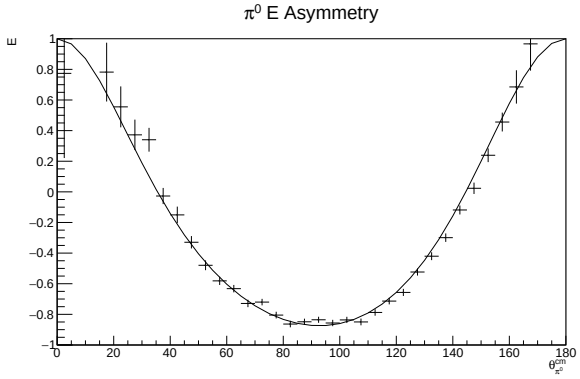

FIG. 16: π^0 E (Σ_{2z}) asymmetry for the 2015 beamtime, with a target polarization correction of 1.25. The curve is the CM12 solution from SAID [10].

times were back-to-back and should therefore have identical factors, all while using expected scale factors for the carbon and helium data. This method results in a higher polarization correction factor than the Bonn group for 2015, but these beamtimes had a complete target shutdown and startup between them, and are therefore not constrained to the same factor. While the use of the helium data in this way appears to work well in describing this additional background for π^0 photoproduction, the data can not be used for the Compton analysis, due to the very limited statistics. Considering this, and the fact that even for the π^0 analysis there are known differences between the beamtimes as described at the beginning of this section, this method serves only as a further confirmation of the need for polarization corrections, and to provide some measure of the uncertainty in these correction factor extractions.

One concern raised is the need in the previous analysis, using carbon data and helium simulation for the subtraction, of an additional carbon subtraction factor. Compared with this analysis, this indicates some compensation of the carbon data for non-coherent processes on helium. The question asked is how does this affect the Compton analysis. Shown in Fig. 17 is the missing mass for Compton scattering at 95°. The carbon data, which are shown in green, have been scaled by this additional factor of ≈ 1.1. The contribution of this background to the distribution below 950 MeV is small, and 10% of that distribution is already within the statistical errors. The contribution is even less at backward angles, as shown in Fig. 18 for 140°. Simulations of these backgrounds on carbon and helium, using some approximate weighting of the cross sections, indicate that the contribution of helium to these distributions below 950 MeV is, coincidentally, approximately 10% of the yield from carbon. Unfortunately, some discrepancies still exist between simulation and data that prevent their full use

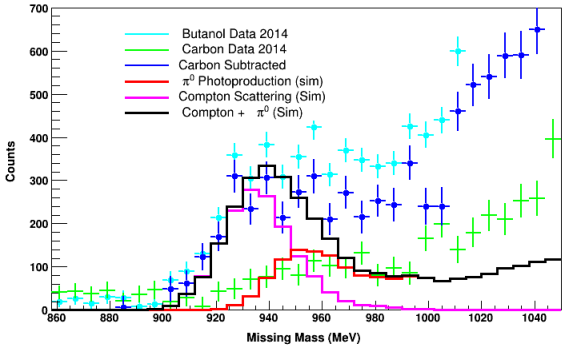

FIG. 17: Compton missing mass at 95° for the 2014 beamtime.

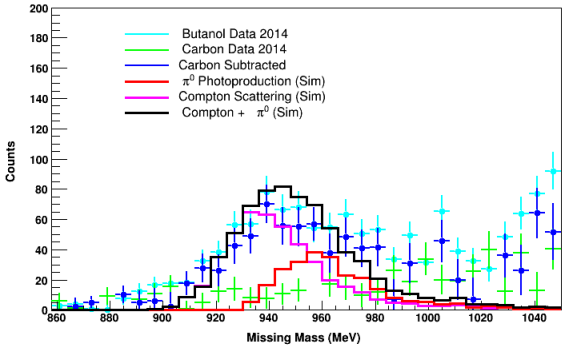

FIG. 18: Compton missing mass at 140° for the 2014 beamtime.

in extracting the signal for Compton scattering on the proton. However, the agreement is adequate to confirm that an additional correction of 10% for the carbon data is both reasonable and accurate, within errors, for the subtraction of backgrounds in the Compton analysis.

V. POLARIZED AND UNPOLARIZED CROSS SECTIONS

The determination of an asymmetry on the longitudinally polarized butanol target, either for the Compton scattering process of interest or for the π^0 photoproduction process used above to extract a polarization correction factor, suffers from one point also addressed above. For the butanol target data, the background contribution from the reactions produced on C, O, and He nuclei could not be fully separated from the polarized H contribution. As these backgrounds from spinless nuclei are not polarization dependent, they cancel when the difference between events in the 3/2 (parallel orientation in Figs. 1a and 1d) and 1/2 (antiparallel orientation in Figs. 1b and 1c) helicity states is taken [13], where 3/2 and 1/2 indicate the relative nucleon-photon spin configuration for parallel and anti-parallel configurations, respectively. The total cross section for parallel ($\sigma^{3/2}$) and anti-parallel ($\sigma^{1/2}$) configurations can be written in terms of unpolarized cross section (σ_0) as,

$$\sigma^{3/2} = \sigma_0 + P_z^t \times P_{circ}^{\gamma} \times A, \tag{4}$$

$$\sigma^{1/2} = \sigma_0 - P_z^t \times P_{circ}^{\gamma} \times A. \tag{5}$$

The cross section difference ($\Delta\sigma$) between these two helicity states can be written as

$$\Delta\sigma = \sigma^{3/2} - \sigma^{1/2} = 2 \times P_z^t \times P_{circ}^{\gamma} \times A. \tag{6}$$

On the other hand, the cross section sum ($\Sigma\sigma$) of the two helicity states cancels out the polarization dependent term, leaving only the unpolarized cross section.

$$\Sigma\sigma = \sigma^{3/2} + \sigma^{1/2} = 2 \times \sigma_0 \tag{7}$$

For this reason, in the following text the sum of the cross sections will be called the "unpolarized" cross section, and the difference will be called the "polarized" cross section (despite this not being entirely accurate).

Using these two calculations, a cross check of the polarization correction determined above can be provided. Two reactions were studied, the single π^0 photoproduction and the total inclusive cross section, accounting for any and all photoreactions on the target. The analysis method for selecting single π^0 photoproduction is the same as used in the asymmetry analysis outlined previously. The analysis method for a total inclusive analysis entails simply counting hits in the tagger, after accounting for accidentals with the typical sideband subtraction.

Figs. 19 and 20 show the total inclusive unpolarized and polarized cross section results, respectively, from the 2014 and 2015 beamtimes. The polarized cross section results are also compared with previous data taken to extract the Gerasimov-Drell-Hearn (GDH) sum rule [14].

Similarly, the unpolarized and polarized π^0 cross section results from the 2014 and 2015 beamtimes are shown in Figs. 21 and 22, respectively. The polarized π^0 cross section results are compared with similar GDH data, as well as with the SAID CM12 solution [10].

It is notable that both the total inclusive and π^0 polarized cross sections for 2014 appear high compared to the GDH data. This would seem to verify that the polarization values used are incorrect. However, the 2015 cross sections appear low compared to the GDH data. While a lower than actual polarization measurement is realistic, a higher than actual measurement is unexplainable. However, the unpolarized cross sections

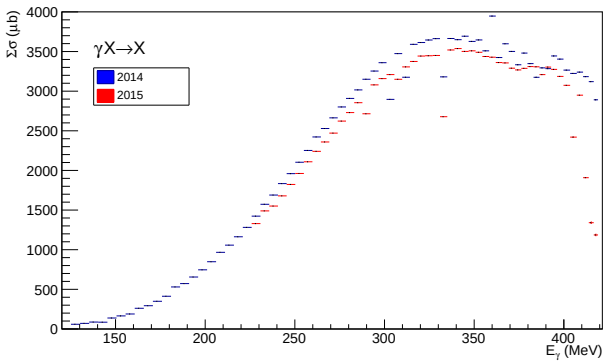

FIG. 19: Unpolarized total inclusive cross section results for 2014 (blue) and 2015 (red) beamtimes.

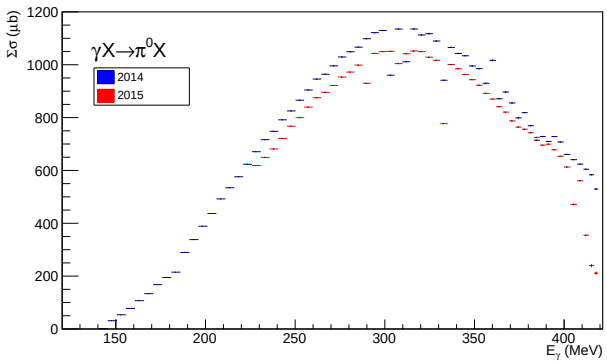

FIG. 21: Unpolarized π^0 cross section results for 2014 (blue) and 2015 (red) beamtimes.

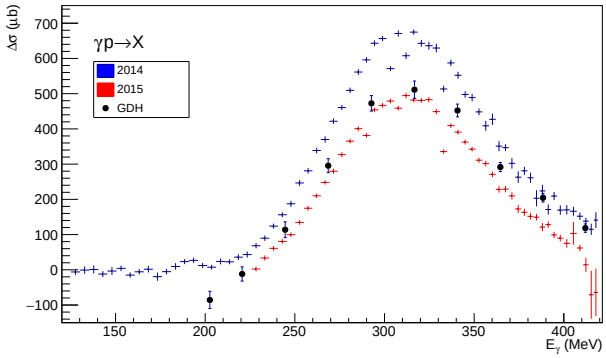

FIG. 20: Polarized total inclusive cross section results for 2014 (blue) and 2015 (red) beamtimes, along with previous GDH data (black circles).

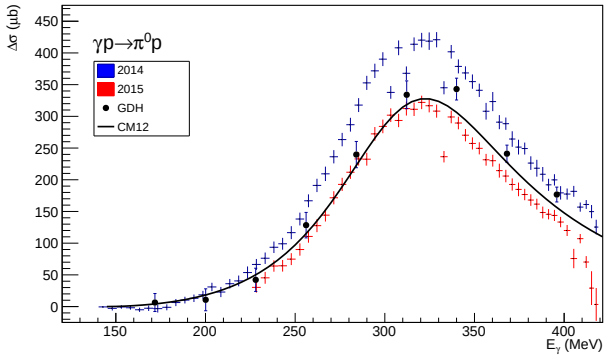

FIG. 22: Polarized π^0 cross section results for 2014 (blue) and 2015 (red) beamtimes, along with previous GDH data (black circles), and the SAID CM12 solution (black line).

for 2015 also appear low with respect to their 2014 counterparts. Since these by definition are not influenced by the target polarization, another effect must be the cause. The difficulty with a cross section calculation, as opposed to an asymmetry, is the need to account for the photon flux, target density, target length, and detection efficiencies. While the photon flux is determined for each beamtime separately, the other three: target density, target length, and detection efficiencies are determined only once for all the beamtimes. Therefore, if one of those values changed for 2015 as compared to the 2014, this would result in a decrease in both the unpolarized and polarized cross sections for 2015. While there is no comparison with previous data or theory for the unpolarized cross sections, as they are determined for the total helium immersed butanol target, the unpolarized 2015 cross sections can at least be scaled up to match the 2014 results. This scale factor can be determined by simply taking the ratio of the 2014 to 2015 data, as shown in Fig. 23. Assuming the need for a scale factor arises from a change in the tagging efficiency, target density, or other quantity that is independent of the incoming photon energy, E_γ, it is reasonable to simply fit these ratios with a flat line. To improve this fit, several channels were manually removed where that channel was significantly discrepant from its neighbors in either 2014 or 2015, as this then led to an unreasonable scale factor for that channel. This fitting then gives scale factors of 1.058 and 1.074 for the total inclusive and π^0 reactions, respectively. Figs. 24 and 25 show the total inclusive and π^0 unpolarized cross section results from the 2014 and 2015 beamtimes, respectively, where these scaling factors have been applied to the 2015 data.

To determine the polarization related scaling factor, the ratio of the 2014 to 2015 polarized cross sections can also be constructed, after first applying the previous scale factor to the 2015 data. This ratio is shown in Fig. 26, and again fit with a simple straight line as a polarization scale factor should be energy independent. The extracted factors were then used to scale just the polarized cross sections for the 2014 beamtime.

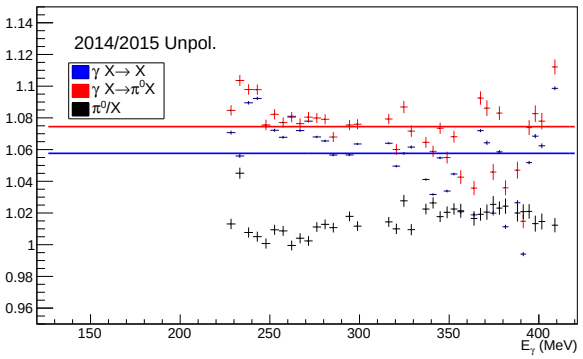

FIG. 23: Ratio of 2014/2015 unpolarized cross section results for total inclusive (blue) and π^0 production (red), as well as the ratio of these two ratios (black).

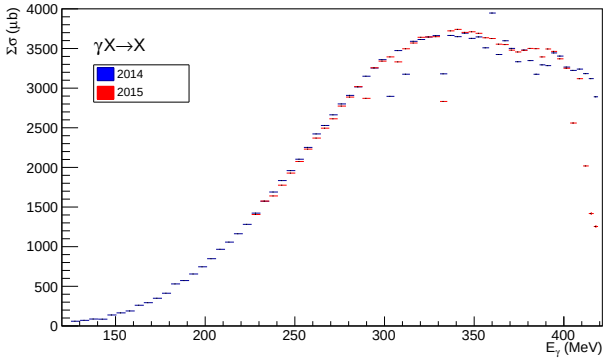

FIG. 24: Unpolarized total inclusive cross section results for 2014 (blue) and 2015 (red) beamtimes, where the latter is scaled by 1.058.

The polarization scale factors for the 2014 beamtime were determined to be 1.323 for the total inclusive case, and 1.256 for the π^0 production case, the latter in clear agreement with the π^0 asymmetry analysis performed above. With both of the 2014 and 2015 scaling factors applied, the polarized data is now in good agreement with the GDH data, as well as with SAID in the case of π^0 photoproduction, as shown in Figs. 27 and 28, for the total inclusive and π^0 production cases respectively.

One concern with this method is that the extracted polarization scale factors are different between the total inclusive and π^0 production cases, which obviously shouldn't be the case. Looking into where this discrepancy might arise, the non-linearity of the distributions in Fig. 26 is worrisome. The shapes of the distributions seem to suggest that applying an offset to either the 2014 or 2015 data before taking the ratio might flatten them. This was confirmed by adding 40 μb and 10 μb to the 2015 polarized total inclusive and π^0 production

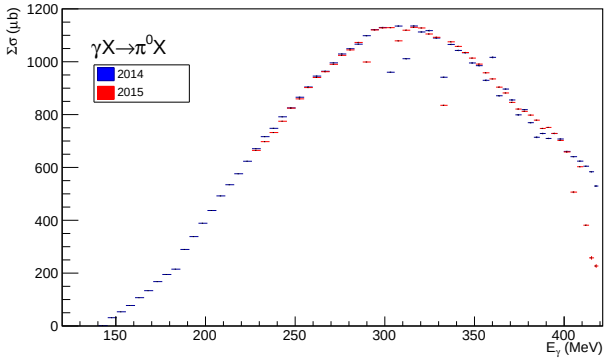

FIG. 25: Unpolarized π^0 cross section results for 2014 (blue) and 2015 (red) beamtimes, where the latter is scaled by 1.074.

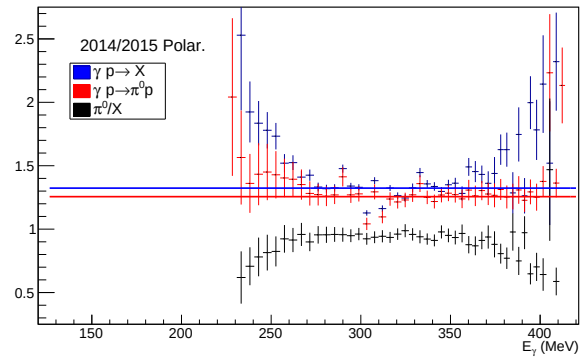

FIG. 26: Ratio of 2014/2015 polarized cross section results for total inclusive (blue) and π^0 production (red), as well as the ratio of these two ratios (black).

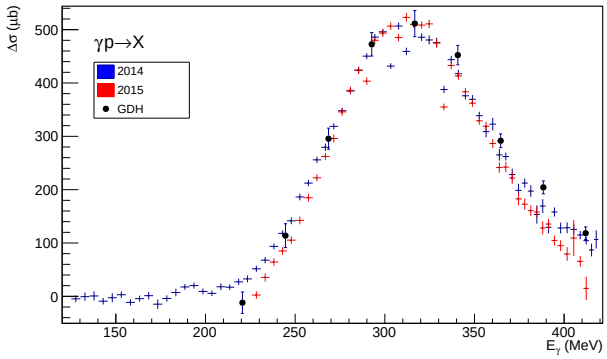

FIG. 27: Polarized total inclusive cross section results for 2014 (blue) and 2015 (red) beamtimes, where the former is scaled by 1.323 and the latter by 1.058, along with previous GDH data (black circles).

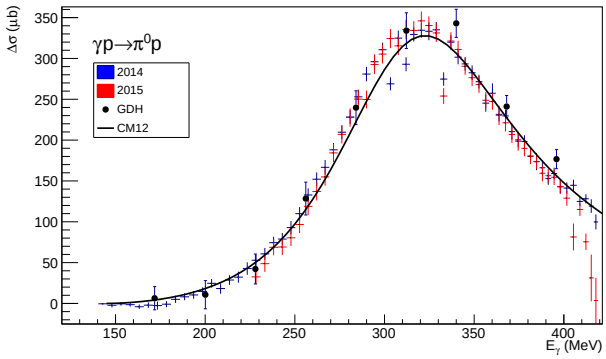

FIG. 28: Polarized π^0 cross section results for 2014 (blue) and 2015 (red) beamtimes, where the former is scaled by 1.256 and the latter by 1.074, along with previous GDH data (black circles), and the SAID CM12 solution (black line).

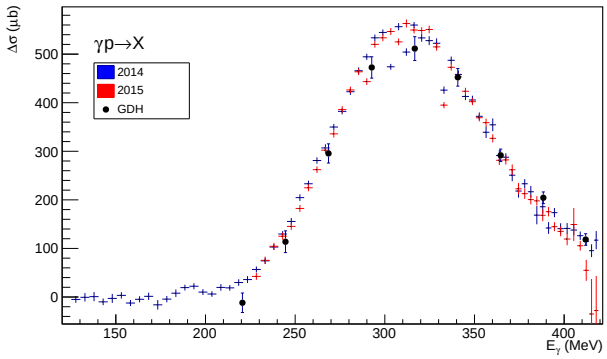

FIG. 30: Polarized total inclusive cross section results for 2014 (blue) and 2015 (red) beamtimes, where the former is scaled by 1.205 and the latter by 1.058 plus a shift of 40 μb, along with previous GDH data (black circles).

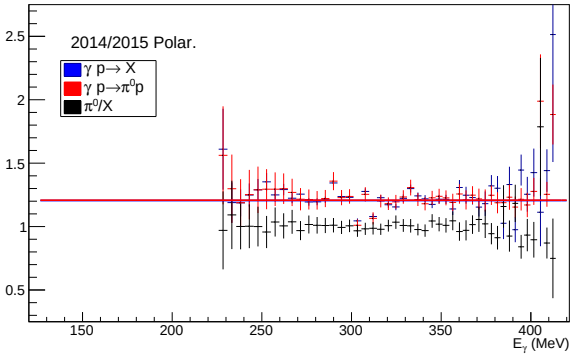

FIG. 29: Ratio of 2014/2015 polarized cross section results for total inclusive (blue) and π^0 production (red), after applying 40 μb and 10 μb shifts, respectively, as well as the ratio of these two ratios (black).

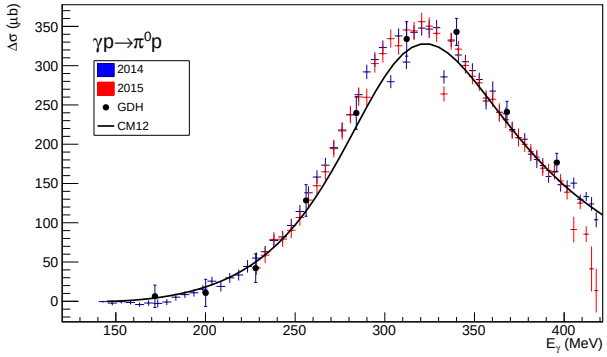

FIG. 31: Polarized π^0 cross section results for 2014 (blue) and 2015 (red) beamtimes, where the former is scaled by 1.208 and the latter by 1.074 plus a shift of 10 μb, along with previous GDH data (black circles), and the SAID CM12 solution (black line).

cross sections, respectively. Taking the ratios with these data results in flatter distributions, as shown in Fig. 29.

In addition to the flatter distributions, the extracted polarization scale factors of 1.205 and 1.208 for the total inclusive and π^0 production cases, respectively, are in excellent agreement. Applying these shifts and scales to the data results in Figs. 30 and 31.

While the π^0 production results in Fig. 31 still agree well with both the GDH data and the SAID CM12 solution, the total inclusive results in Fig. 30 are now high with respect to the GDH data in the region around the peak. Regardless, simply shifting the cross sections by these amounts is not justifiable from the analysis standpoint. Initially done as a curiosity, it does however give some indication of the size of the systematic error that should be included with any polarization scale factor derived in this way.

The statistical fitting error is 0.45% and 0.90% for the total inclusive and π^0 production cases, respectively. Although the factor is derived from ratios of cross sections, in which various factors drop out, these factors can be different for each beamtime, so their systematic errors must be accounted for. Combining the relative systematic errors for beam polarization (2.7%), tagging efficiency (3.2%), target area density (3.3%), and detection efficiency (taken as 2%), this results in an 8.1% relative error ($5.7\% \times \sqrt{2}$, as the four multiplicative factors are in the numerator and in the denominator). Taking the polarization scale factor derived from the ratio of π^0 production data (without the 10 μb shift), this gives a factor of $1.256 \pm 0.011\,(\text{stat}) \pm 0.101\,(\text{syst})$, which is

consistent with the other extractions within errors.

A. Comparison of Polarization Correction Factors

The π^0 photoproduction asymmetry Σ_{2z} results discussed in Sec. IV suggest that the target polarization corrections are needed. Tables III and IV show the reported and corrected target polarization values for the 2014 and 2015 beamtimes. The corrected values are as determined by comparison of the asymmetries, calculated with the inclusion of MC simulation of coherent π^0 production on ^{4}He, to theory. These corrections are similar (within the range of uncertainties) to the factors determined from polarized and unpolarized cross section studies discussed in Sec. V. While the systematic uncertainty of a target polarization calculated via the NMR method is about 3%, and the uncertainties on a corrected polarization extracted via the asymmetry or cross section method are roughly 3% and 8%, respectively, a conservative error of 10% will be taken to account for the variations in these factors.

Start date	End date	P_i^T(%)	P_f^T(%)	P_i^{TC}(%)	P_f^{TC}(%)
02.05.2014	12.05.2014	63.6	58.7	80.1	74.0
13.05.2014	19.05.2014	-61.6	-53.7	-77.6	-67.7

TABLE III: Summary of target polarization at the start (P_i^T) and end (P_f^T) of the data taking periods, as determined by[7, 8] (third and fourth columns) and after correction by the factor of 1.26 as determined in Sec. IV (P_i^{TC} and P_f^{TC} in the fifth and sixth columns), for the 2014 beamtime.

Start date	End date	P_i^T(%)	P_f^T(%)	P_i^{TC}(%)	P_f^{TC}(%)
23.06.2015	02.07.2015	74.2	62.7	83.1	70.2
02.07.2015	11.07.2015	-65.2	-49.0	-73.0	-54.9

TABLE IV: Summary of target polarization at the start (P_i^T) and end (P_f^T) of the data taking periods, as determined by Ref. [7] (third and fourth columns) and after correction by the factor of 1.12 as determined in Sec. IV (P_i^{TC} and P_f^{TC} in the fifth and sixth columns), for the 2015 beamtime.

VI. COMPTON Σ_{2z} ASYMMETRY

The Σ_{2z} Compton asymmetry was evaluated by applying various kinematic cuts, including the cut on the missing mass distribution as discussed in Ref. [2]. The choice of cut on the upper missing mass limit causes a change in the Compton yield, with a narrow cut eliminating more background but also resulting in a loss of some useful events. A wider cut retains more events, but has a higher possibility of including background. The lower limit in the missing mass cut is 900 MeV in each bin. The ratio of π^0 photoproduction to Compton scattering, from a fit of simulation line-shapes, was used to determine the upper limit in the missing mass cut in each bin. The reanalysis of the additional carbon scaling factor, as discussed in Sec. III C 2, resulted in tighter missing mass cuts and larger statistical uncertainties compared to [2]. See Appendix D for details on the updated upper cuts in the missing mass. To extract the systematic uncertainty, the standard cut positions discussed in Appendix D were changed by ±5 MeV and the Σ_{2z} asymmetry was calculated to extract the relative difference. The shift on the asymmetries was random, i.e. varied up and down randomly from bin-to-bin. This random shift was evaluated to be $\approx \pm 10\%$.

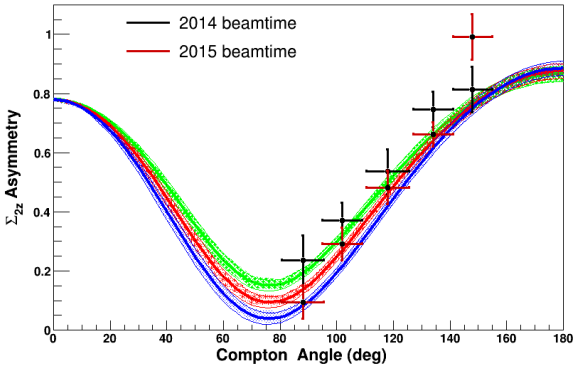

FIG. 32: Compton Σ_{2z} asymmetry, without target polarization correction factors applied, from the 2014 and 2015 beamtimes at $E_\gamma = 285 - 305$ MeV. Only the random (point-to-point) errors are shown. The curves are from the HDPV dispersion theory calculation of Pasquini, *et al.*, [19, 20], where γ_{E1E1} is fixed at -4.3×10^{-4} fm^4 and γ_{M1M1} is set at 2.9, 3.9 and 4.9×10^{-4} fm^4, in the green, red, and blue bands, respectively. The width of each band represents the other parameters, γ_0, γ_π, $\alpha_{E1} + \beta_{M1}$ and $\alpha_{E1} - \beta_{M1}$ varying within their experimental errors.

Fig. 32 shows Σ_{2z} Compton asymmetry results at $E_\gamma = 285 - 305$ MeV from the 2014 and 2015 beamtimes. The curves are from the fixed-t HDPV dispersion theory calculation of Pasquini et al. [19, 20]. See Ref. [2] for details.

Fig. 33 shows the same asymmetry results, but after applying the polarization correction factors discussed in Sec. III C 3.

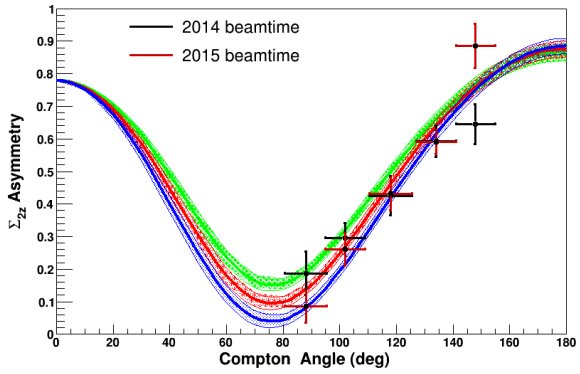

FIG. 33: Compton Σ_{2z} asymmetry, with target polarization correction factors applied, from the 2014 and 2015 beamtimes at $E_\gamma = 285 - 305$ MeV. Otherwise same description as Fig. 32.

The weighted average of the Compton Σ_{2z} asymmetries from the two beamtimes are shown in Fig. 34. The uncertainties were handled by separating them into random (point-to-point) and systematic (correlated) uncertainties. The non-statistical uncertainties are: target polarization (10%), beam polarization (2.7%), carbon scaling factor $(4 - 6\%)$, and missing mass integration limit. While the first three are correlated for the measurement of the Σ_{2z} asymmetry, this is not so for the fourth. Since the uncertainty from the cut on the reconstructed proton missing mass is completely random, they are summed in quadrature with the statistical uncertainty, as shown in Table VII, and included in the weighted average of the 2014 and 2015 beamtimes as given in Table V. On the other hand, the systematic uncertainties from the first three sources were added in quadrature (last column of Table VII in Appendix) and are then plotted as a separate block histogram as shown in Fig. 34.

VII. SUMMARY

In summary, the target correction factors determined, including simulation of coherent π^0 production on ^{4}He (Sec. III C 3) and from helicity dependent cross section studies (Sec. V), agree within the statistical uncertainties. This indicates that there are no systematic effects or flaws in the methodology of the data analysis. The agreement suggests that both the simulation of coherent π^0 production on ^{4}He and the helicity dependent cross section difference and sum can be used to investigate inconsistencies in target polarization values. The target polarization corrections determined from the analysis of the π^0 longitudinal target asymmetry, utilizing the simulation of coherent π^0 production on ^{4}He as discussed in Sec. IV were chosen to apply in the analysis of the Compton scattering asymmetries.

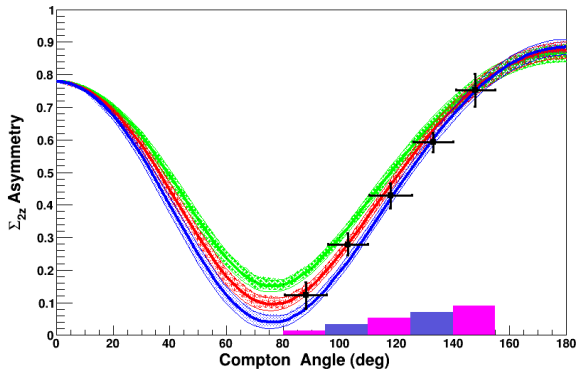

FIG. 34: Weighted average of Σ_{2z} Compton asymmetry final results from the 2014 and 2015 beamtimes at $E_\gamma = 285 - 305$ MeV. Otherwise same description as Fig. 32.

E_γ (MeV)	θ_γ	Σ_{2z}	Rand.	Syst.
265–285	87.5°	0.193	0.056	0.024
	102.5°	0.290	0.040	0.035
	117.5°	0.402	0.037	0.048
	132.5°	0.672	0.036	0.077
	147.5°	0.672	0.042	0.081
285–305	87.5°	0.121	0.040	0.016
	102.5°	0.279	0.034	0.033
	117.5°	0.428	0.038	0.048
	132.5°	0.591	0.029	0.066
	147.5°	0.751	0.046	0.085
310–330	87.5°	0.394	0.047	0.048
	102.5°	0.597	0.044	0.073
	117.5°	0.638	0.040	0.074
	132.5°	0.664	0.037	0.078
	147.5°	0.711	0.048	0.083

TABLE V: Summary of results and uncertainties for the Compton Σ_{2z} asymmetry.

[1] G. Reicherz, Collaboration meeting presentation, https://wwwa2.kph.uni-mainz.de/intern/daqwiki/meetings/collaboration_meetings/2016_03/start.

[2] D. Paudyal, Ph.D thesis, University of Regina (2017), http://wwwa2.kph.uni-mainz.de/images/publications/phd/Paudyal-PhD-thesis.pdf.
[3] C. Collicott, *et al.*, in preparation (2018).
[4] P. Martel, *et al.*, Phys. Rev. Lett. **114**, 102501 (2015).
[5] J. Linturi, Internal Report, University of Mainz (2014), https://wwwa2.kph.uni-mainz.de/intern/daqwiki/targetpolarization.pdf.
[6] A. Thomas, Eur. Phys. J. Spec. Top. **198**, 171 (2011).
[7] G. Reicherz, Private Communication.
[8] A. Thomas, Private Communication.
[9] F. Afzal, Private Communication.
[10] http://gwdac.phys.gwu.edu/.
[11] https://maid.kph.uni-mainz.de/.
[12] J. McGeorge, *et al.*, Eur. Phys. J. A **37**, 129 (2008).
[13] J. Ahrens, *et al.*, Phys. Rev. Lett. **84**, 5950 (2000).
[14] J. Ahrens, *et al.*, Phys. Rev. Lett. **87**, 022003 (2001).
[15] V. O. de Leon, *et al.*, Eur. Phys. J. A **10**, 207 (2001).
[16] H. W. Grieβhammer, J. A. McGovern, D. R. Phillips, and G. Feldman, Prog. Part. Nucl. Phys. **67**, 841 (2012).
[17] V. Lensky and V. Pascalutsa, Eur. Phys. J. C **65**, 207 (2010).
[18] S. Kondratyuk, *et al.*, Phys. Rev. C **64**, 024005 (2001).
[19] B. Pasquini, D. Drechsel, and M. Vanderhaeghen, Phys. Rev. C **76**, 015203 (2007).
[20] D. Drechsel, B. Pasquini, and M. Vanderhaeghen, Phys. Rept. C **378**, 99 (2003).

Appendix A MORE COMPTON Σ_{2z} RESULTS

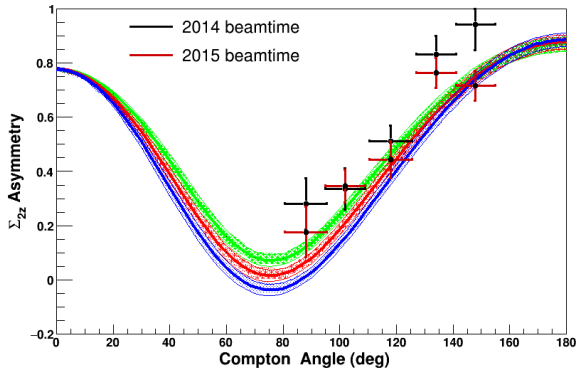

FIG. 35: Compton Σ_{2z} asymmetry (no target polarization correction factor applied) from the 2014 and 2015 beamtime at $E_\gamma = 265 - 285$ MeV. Otherwise same description as Fig. 32.

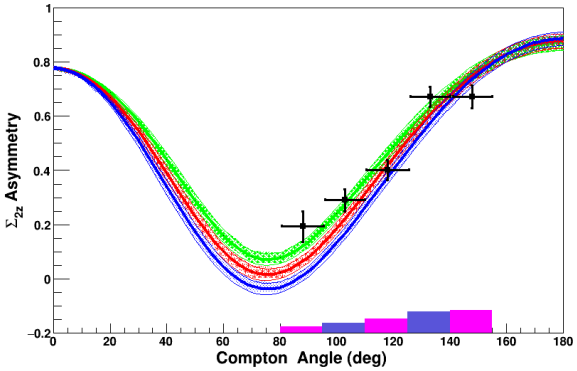

FIG. 37: Weighted average of Σ_{2z} Compton asymmetry results from the 2014 and 2015 beamtimes at $E_\gamma = 265 - 285$ MeV. Otherwise same description as Fig. 32.

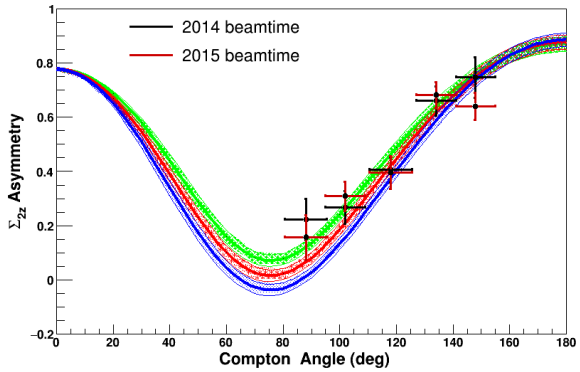

FIG. 36: Compton Σ_{2z} asymmetry with target polarization correction factor applied from the 2014 and 2015 beamtime at $E_\gamma = 265 - 285$ MeV. Otherwise same description as Fig. 32.

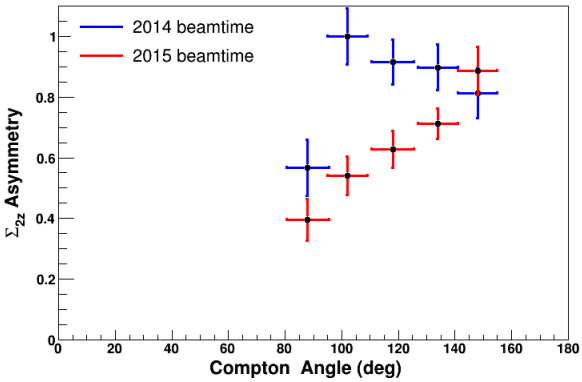

FIG. 38: Compton Σ_{2z} asymmetry without target polarization correction factor applied from the 2014 and 2015 beamtime at $E_\gamma = 310 - 330$ MeV. Otherwise same description as Fig. 32.

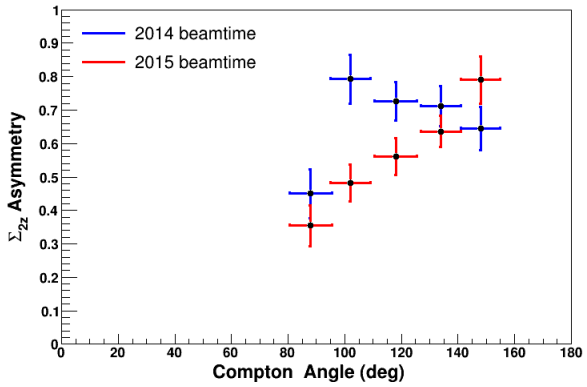

FIG. 39: Compton Σ_{2z} asymmetry with target polarization correction factor applied from the 2014 and 2015 beamtime at $E_\gamma = 310 - 330$ MeV. Otherwise same description as Fig. 32.

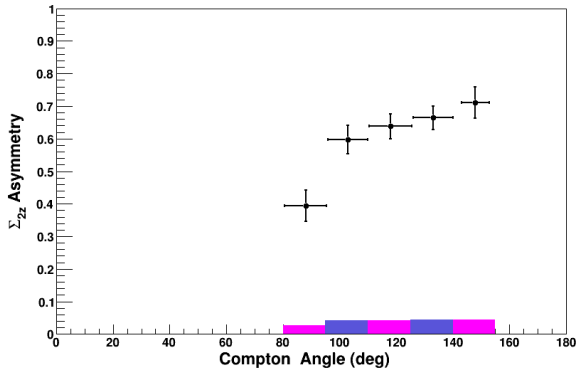

FIG. 40: Weighted average of Σ_{2z} Compton asymmetry results from the 2014 and 2015 beamtimes at $E_\gamma = 310 - 330$ MeV. Otherwise same description as Fig. 32.

Appendix B SYSTEMATIC ERRORS

Appendix C MISSING MASS FOR π^0 PHOTOPRODUCTION EVENTS AT ALL ANGLES

The following naming convention have been used in the following sections.

- P0C0: Positively polarized target (P) with left-handed helicity (0) state of the beam, and carbon target (C) with left-handed helicity (0) state was used in background subtraction.
- P1C1: Positively polarized target (P) with right-handed helicity (1) state of the beam, and carbon target (C) with right-handed helicity (1) state was used in background subtraction.
- N0C0: Negatively polarized target (N) with left-handed helicity (0) state of the beam, and carbon target (C) with left-handed helicity (0) state was used in background subtraction.
- N1C1: Negatively polarized target (N) with right-handed helicity (1) state of the beam, and carbon target (C) with right-handed helicity (1) state was used in background subtraction.

Fig. 43 shows the missing mass spectra for "N0C0" configuration at eighteen angular bins, top left to right: $\theta_{\pi^0} = 0 - 10°, 10 - 20°, 20 - 30°$ and so on. Similarly, the missing mass spectrum for "N1C1", "P0C0" and "P1C1" configurations are shown in Figs. 44–50 respectively.

Appendix D ADDITIONAL PLOTS

Beamtime	θ_γ	Σ_{2z}	Random uncertainties (±)			Systematic uncertainties (±)			
			Stat.	Cut_{MM}	Total	Target	Beam	Carbon	Total
2014	87.5°	0.223	0.072	0.017	0.075	0.022	0.006	0.013	0.027
	102.5°	0.267	0.056	0.021	0.060	0.027	0.007	0.016	0.032
	117.5°	0.406	0.038	0.025	0.046	0.041	0.011	0.021	0.047
	132.5°	0.660	0.026	0.047	0.054	0.066	0.017	0.033	0.076
	147.5°	0.747	0.066	0.036	0.075	0.075	0.020	0.037	0.086
2015	87.5°	0.157	0.082	0.014	0.083	0.016	0.004	0.011	0.020
	102.5°	0.309	0.050	0.022	0.054	0.031	0.008	0.021	0.038
	117.5°	0.396	0.054	0.029	0.061	0.040	0.010	0.026	0.048
	132.5°	0.681	0.037	0.030	0.048	0.068	0.019	0.034	0.078
	147.5°	0.639	0.037	0.034	0.050	0.064	0.017	0.037	0.076

TABLE VI: Summary of results and uncertainties for the Compton Σ_{2z} asymmetry, with additional target polarization scaling, at $E_\gamma = 265 - 285$ MeV.

Beamtime	θ_γ	Σ_{2z}	Random uncertainties (±)			Systematic uncertainties (±)			
			Stat.	Cut_{MM}	Total	Target	Beam	Carbon	Total
2014	87.5°	0.187	0.066	0.015	0.067	0.019	0.005	0.010	0.022
	102.5°	0.295	0.040	0.024	0.047	0.029	0.008	0.015	0.034
	117.5°	0.425	0.054	0.027	0.060	0.043	0.011	0.017	0.047
	132.5°	0.593	0.035	0.033	0.048	0.059	0.016	0.023	0.066
	147.5°	0.646	0.053	0.031	0.061	0.065	0.017	0.026	0.072
2015	87.5°	0.085	0.050	0.008	0.050	0.009	0.003	0.004	0.010
	102.5°	0.261	0.044	0.023	0.050	0.026	0.007	0.016	0.031
	117.5°	0.430	0.039	0.030	0.050	0.043	0.012	0.017	0.048
	132.5°	0.590	0.029	0.037	0.037	0.059	0.016	0.023	0.065
	147.5°	0.885	0.055	0.041	0.069	0.089	0.024	0.035	0.098

TABLE VII: Summary of results and uncertainties for the Compton Σ_{2z} asymmetry, with additional target polarization scaling, at $E_\gamma = 285 - 305$ MeV.

Beamtime	θ_γ	Σ_{2z}	Random uncertainties (±)			Systematic uncertainties (±)			
			Stat.	Cut_{MM}	Total	Target	Beam	Carbon	Total
2014	87.5°	0.450	0.064	0.036	0.073	0.045	0.012	0.022	0.052
	102.5°	0.793	0.035	0.064	0.073	0.079	0.021	0.040	0.091
	117.5°	0.726	0.041	0.040	0.058	0.073	0.020	0.037	0.084
	132.5°	0.712	0.038	0.045	0.060	0.071	0.019	0.036	0.082
	147.5°	0.645	0.057	0.031	0.065	0.065	0.017	0.033	0.074
2015	87.5°	0.354	0.053	0.031	0.062	0.035	0.010	0.024	0.044
	102.5°	0.482	0.037	0.043	0.056	0.048	0.013	0.024	0.055
	117.5°	0.561	0.037	0.040	0.054	0.056	0.015	0.028	0.064
	132.5°	0.636	0.030	0.034	0.046	0.064	0.017	0.032	0.073
	147.5°	0.790	0.056	0.042	0.071	0.079	0.021	0.039	0.091

TABLE VIII: Summary of results and uncertainties for the Compton Σ_{2z} asymmetry, with additional target polarization scaling, at $E_\gamma = 310 - 330$ MeV.

Beamtime	Compton Angular Range	Missing Mass Upper Limit		
		$E_\gamma = 265 - 285$ MeV	$E_\gamma = 285 - 305$ MeV	$E_\gamma = 310 - 330$ MeV
2014	$80 - 95^\circ$	945	948	945
	$95 - 110^\circ$	942	945	945
	$110 - 125^\circ$	943	944	942
	$125 - 140^\circ$	940	942	942
	$140 - 150^\circ$	941	942	945
2015	$80 - 95^\circ$	944	945	945
	$95 - 110^\circ$	941	941	940
	$110 - 125^\circ$	940	942	942
	$125 - 140^\circ$	940	942	940
	$140 - 150^\circ$	940	940	941

TABLE IX: Missing mass cuts determined for three energy and five angular bins of Compton scattering. The upper missing mass limits are based on π^0 photoproduction taken as a reference and detailed Compton Σ_{2z} asymmetry versus upper missing mass limit study.

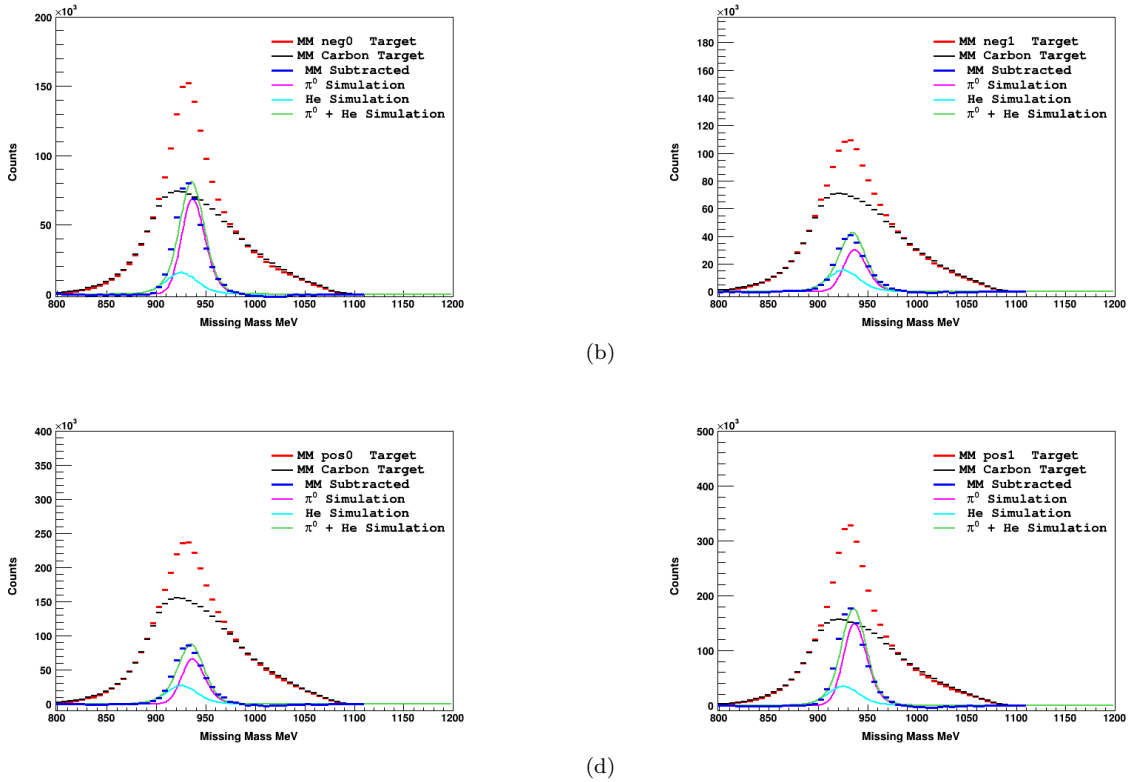

FIG. 41: Missing mass from π^0 photoproduction events over all π^0 angles, and $E_\gamma = 310 - 330$ MeV from the 2014 beamtime. These are the four-fold analysis results on (a) N0CO, (b) N1C1, (c) P0CO and (d) P1C1 parallel and anti-parallel configurations (different target polarization and beam helicity states) as discussed in Sec. III D.

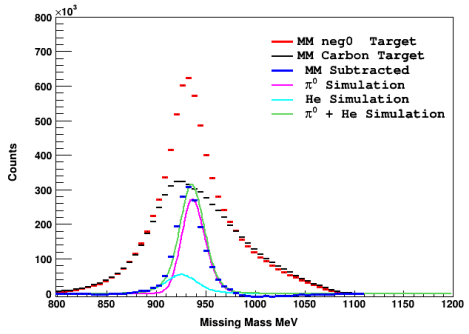

(a)

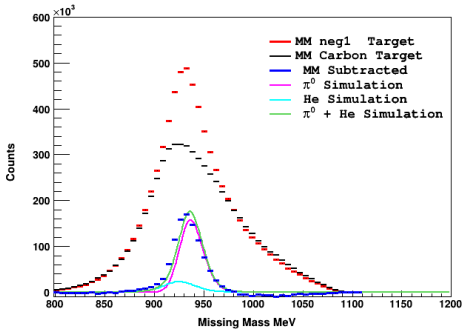

(b)

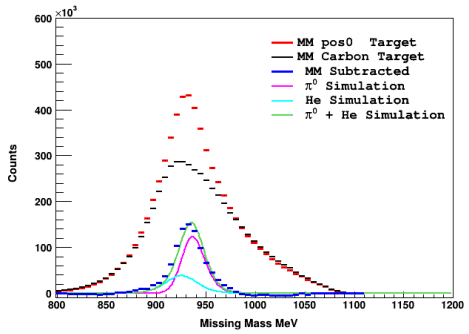

(c)

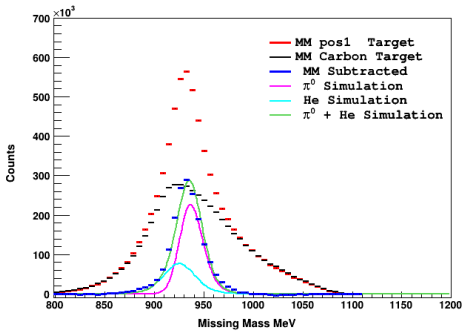

(d)

FIG. 42: Missing mass from π^0 photoproduction events over all π^0 angles, and $E_\gamma = 310 - 330$ MeV from the 2015 beamtime. These are the four-fold analysis results on (a) N0CO, (b) N1C1, (c) P0CO and (d) P1C1 parallel and anti-parallel configurations (different target polarization and beam helicity states) as discussed in Sec. III D.

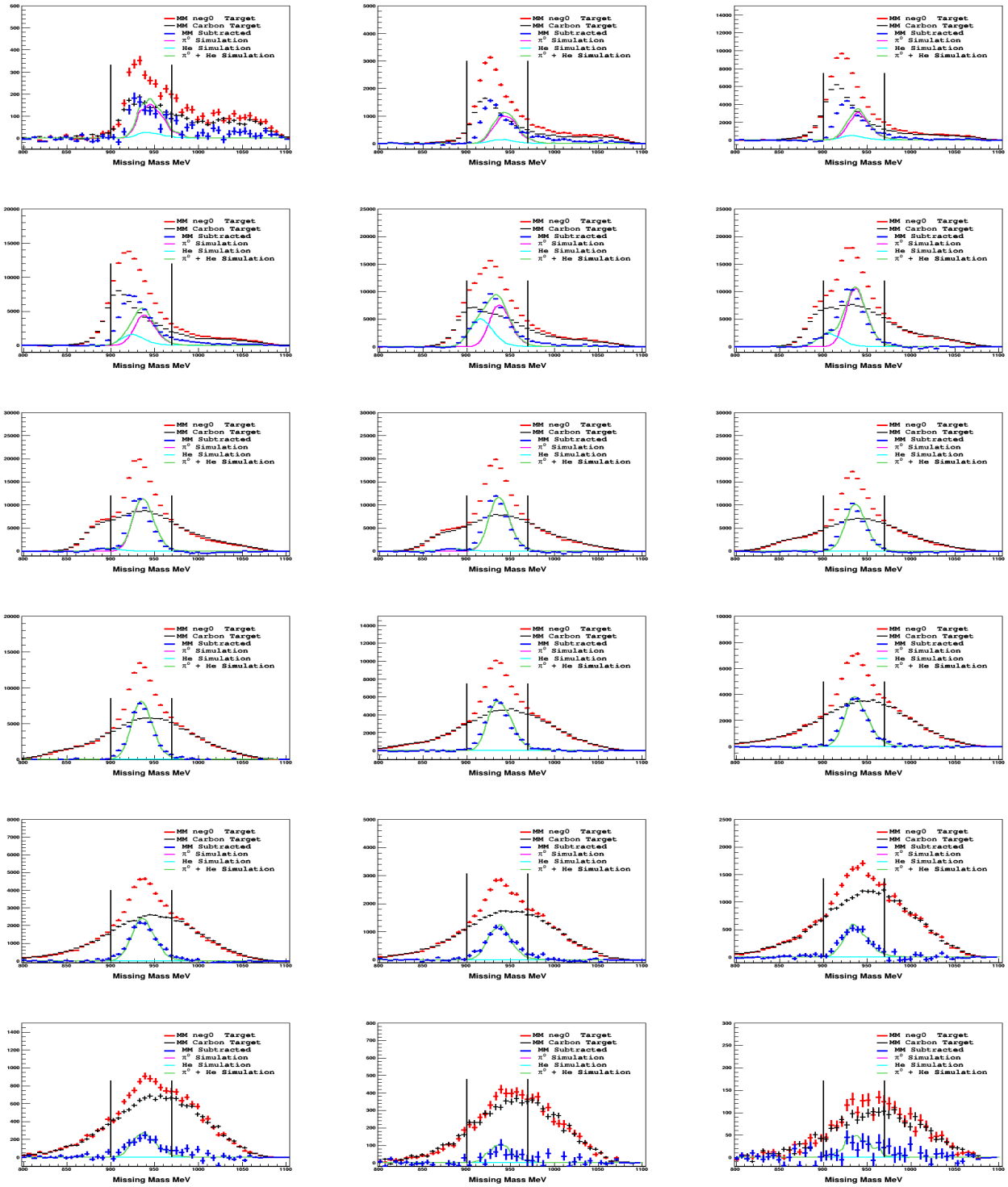

FIG. 43: Missing mass spectrum at $\theta_{\pi^0} = 0-10°, 10-20°, \ldots, 170-180°$ and $E_\gamma = 310-330$ MeV on the π^0 photoproduction channel from the 2014 beamtime. The two vertical lines represent the missing mass integration limit (N0C0).

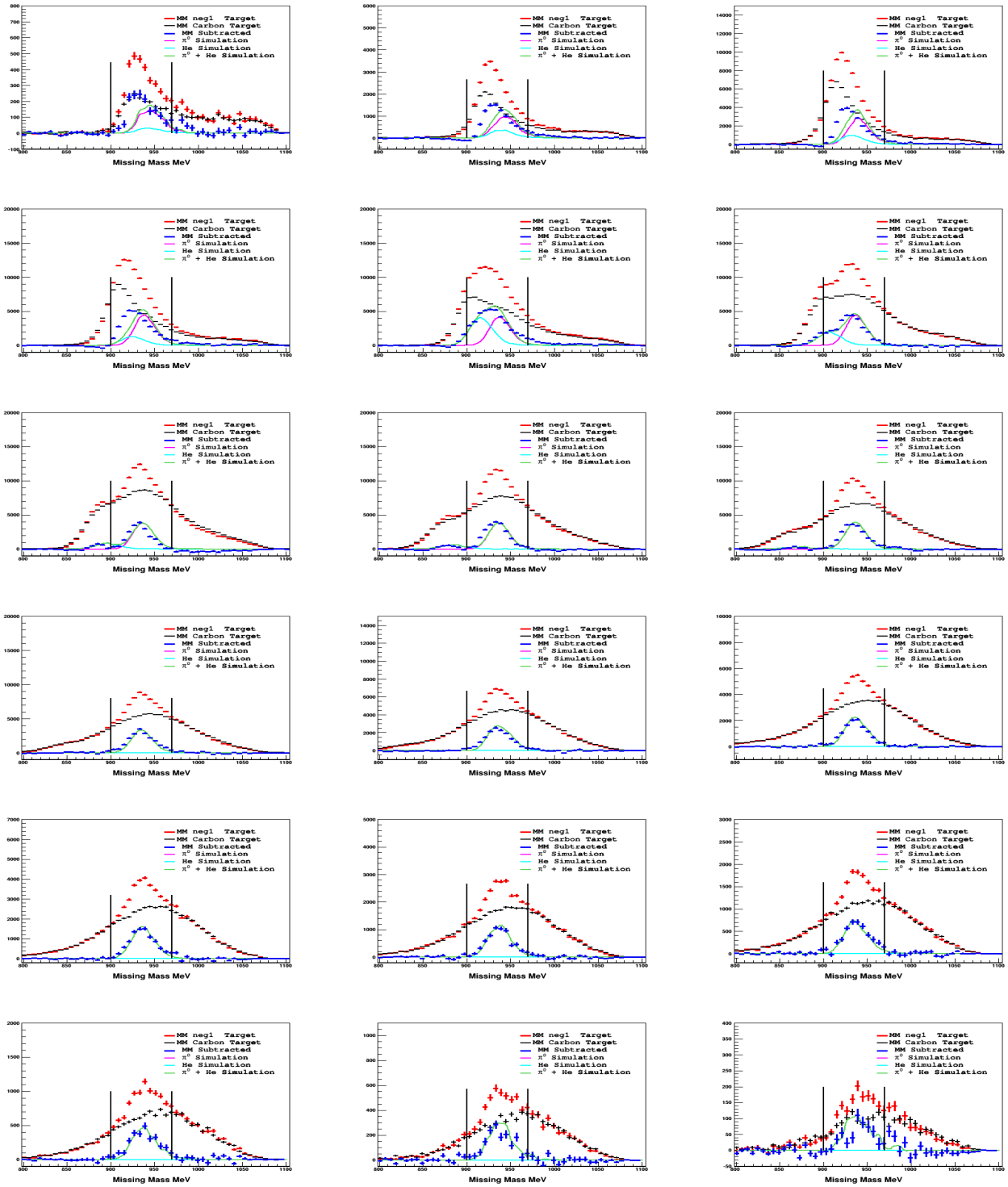

FIG. 44: Missing mass spectrum at $\theta_{\pi^0} = 0-10°, 10-20°, \ldots, 170-180°$ and $E_\gamma = 310-330$ MeV on the π^0 photoproduction channel from the 2014 beamtime. The two vertical lines represent the missing mass integration limit (N1C1).

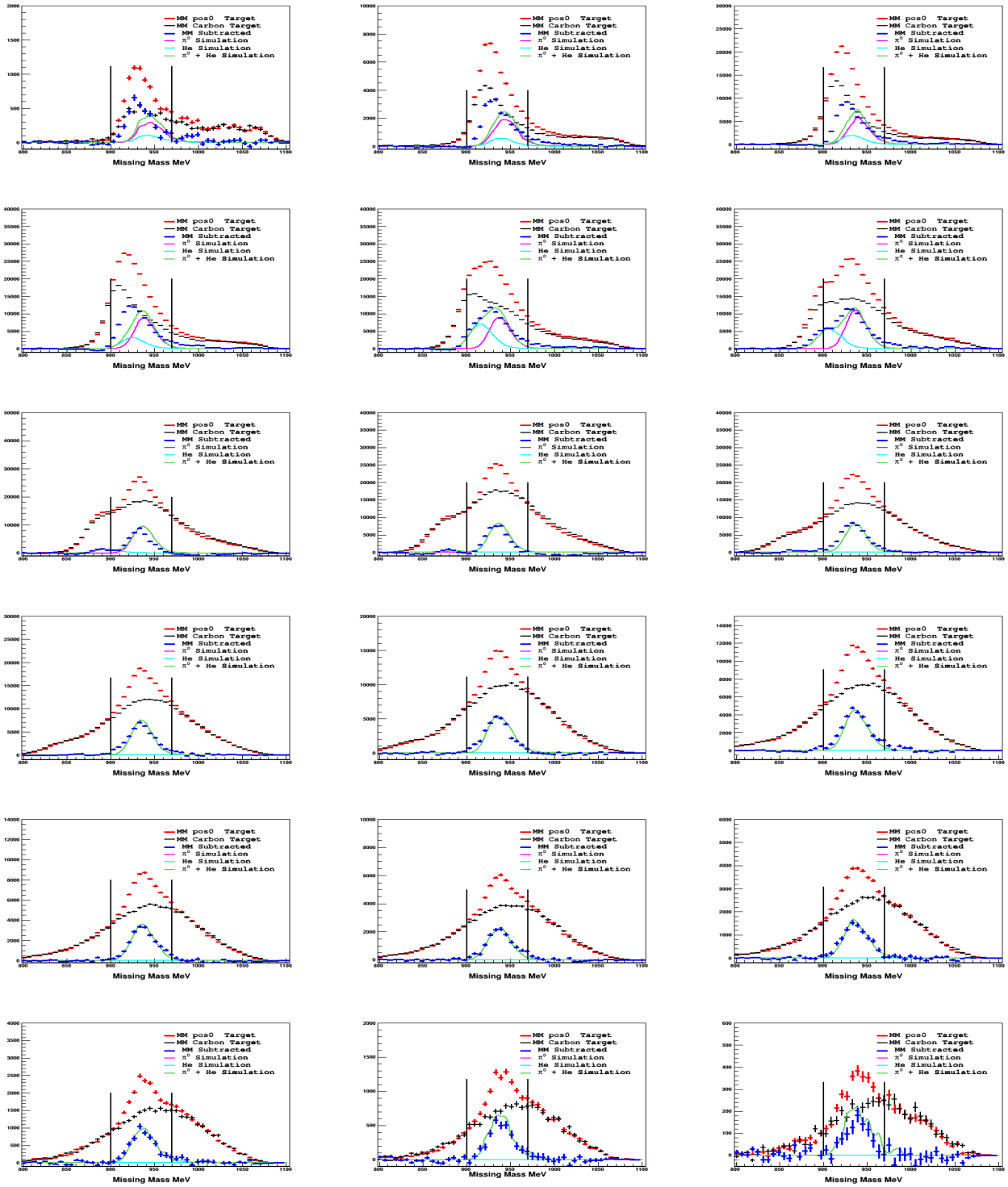

FIG. 45: Missing mass spectrum at $\theta_{\pi^0} = 0-10°, 10-20°, \ldots, 170-180°$ and $E_\gamma = 310-330$ MeV on the π^0 photoproduction channel from the 2014 beamtime. The two vertical lines represent the missing mass integration limit (P0C0).

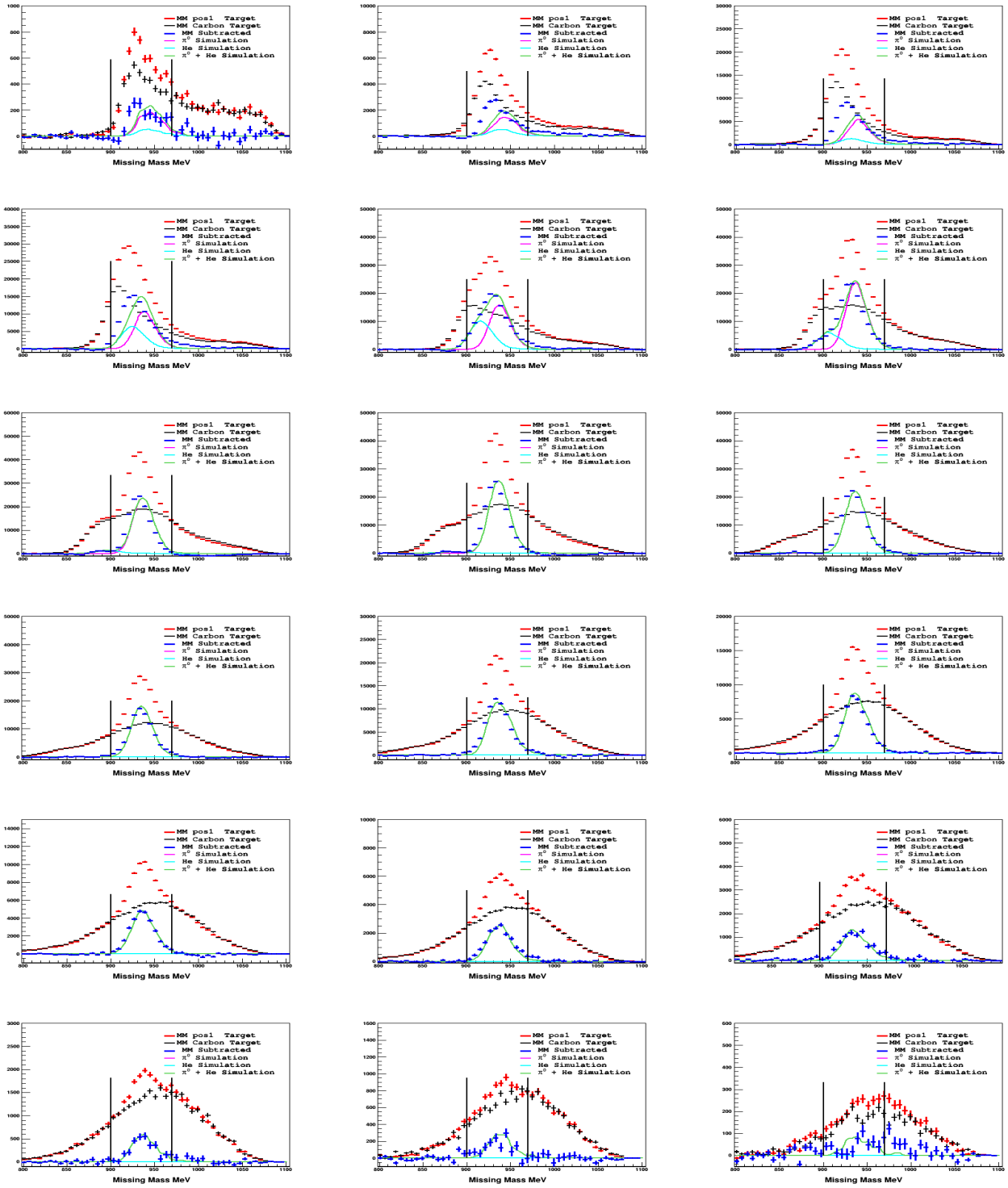

FIG. 46: Missing mass spectrum at $\theta_{\pi^0} = 0 - 10°, 10james14 - 20°, \ldots, 170 - 180°$ and $E_\gamma = 310 - 330$ MeV on the π^0 photoproduction channel from the 2014 beamtime. The two vertical lines represent the missing mass integration limit (P1C1).

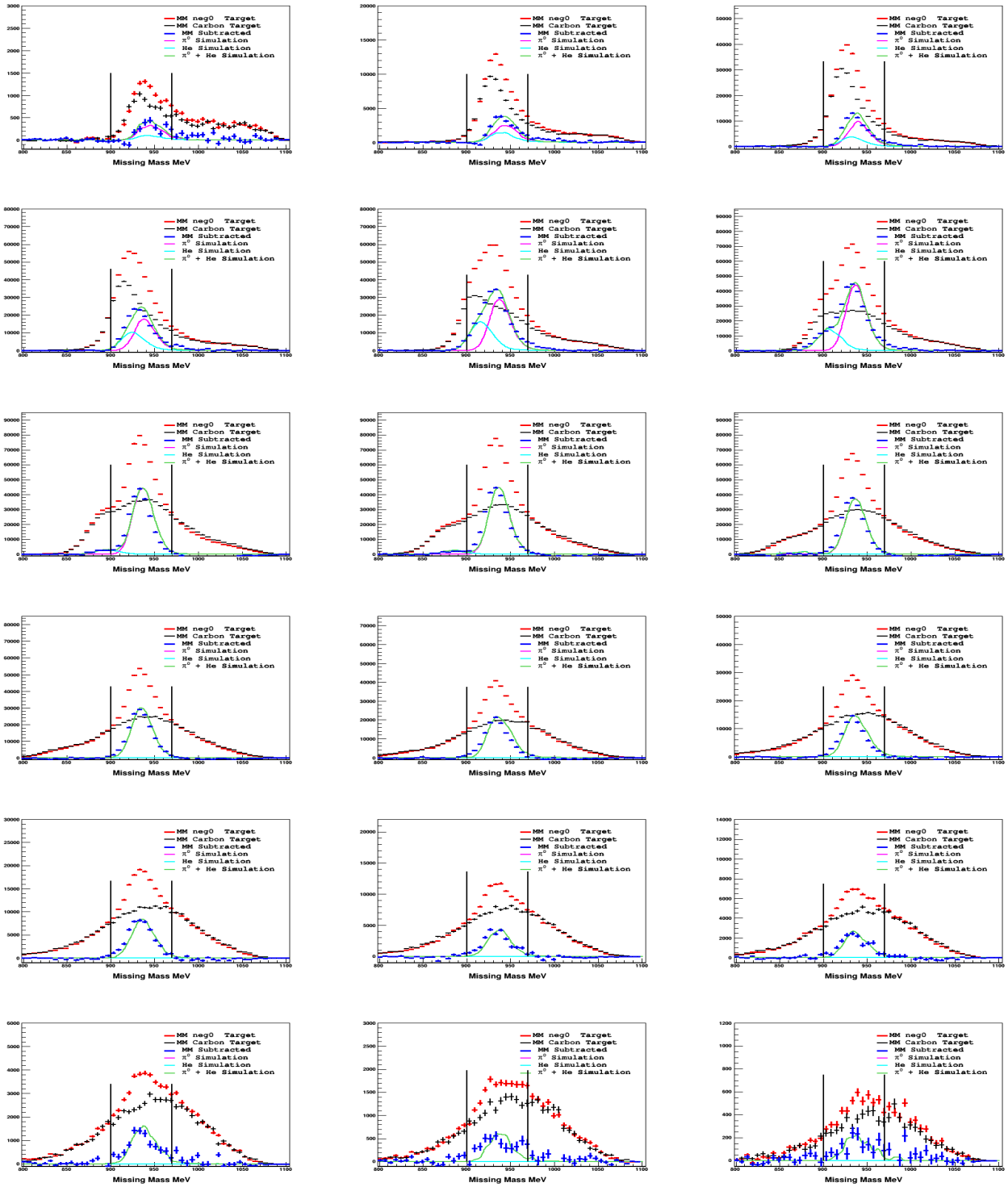

FIG. 47: Missing mass spectrum at $\theta_{\pi^0} = 0-10°, 10-20°, \ldots, 170-180°$ and $E_\gamma = 310-330$ MeV on the π^0 photoproduction channel from the 2015 beamtime. The two vertical lines represent the missing mass integration limit (N0C0).

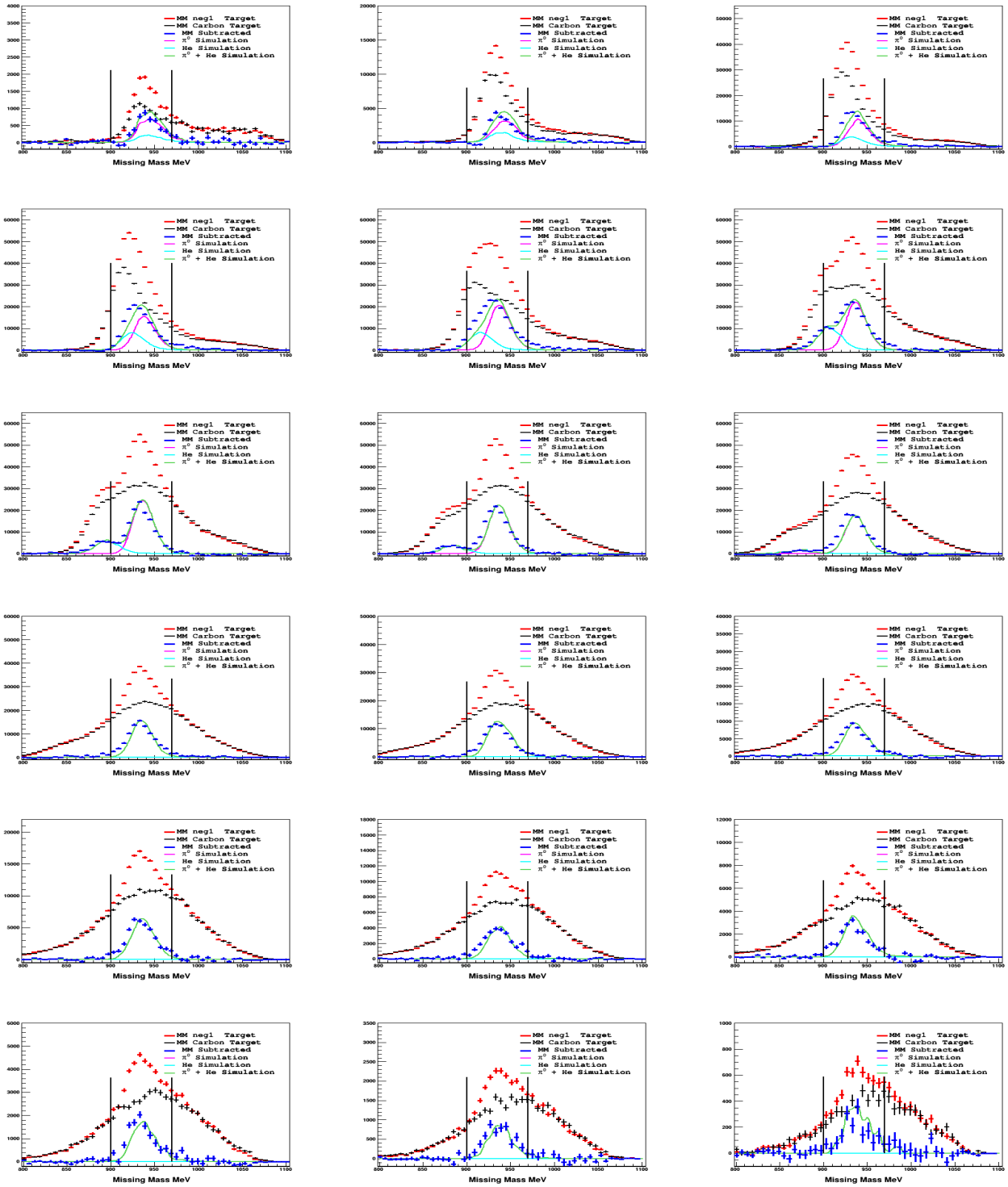

FIG. 48: Missing mass spectrum at $\theta_{\pi^0} = 0-10°, 10-20°, \ldots, 170-180°$ and $E_\gamma = 310-330$ MeV on the π^0 photoproduction channel from the 2015 beamtime. The two vertical lines represent the missing mass integration limit (N1C1).

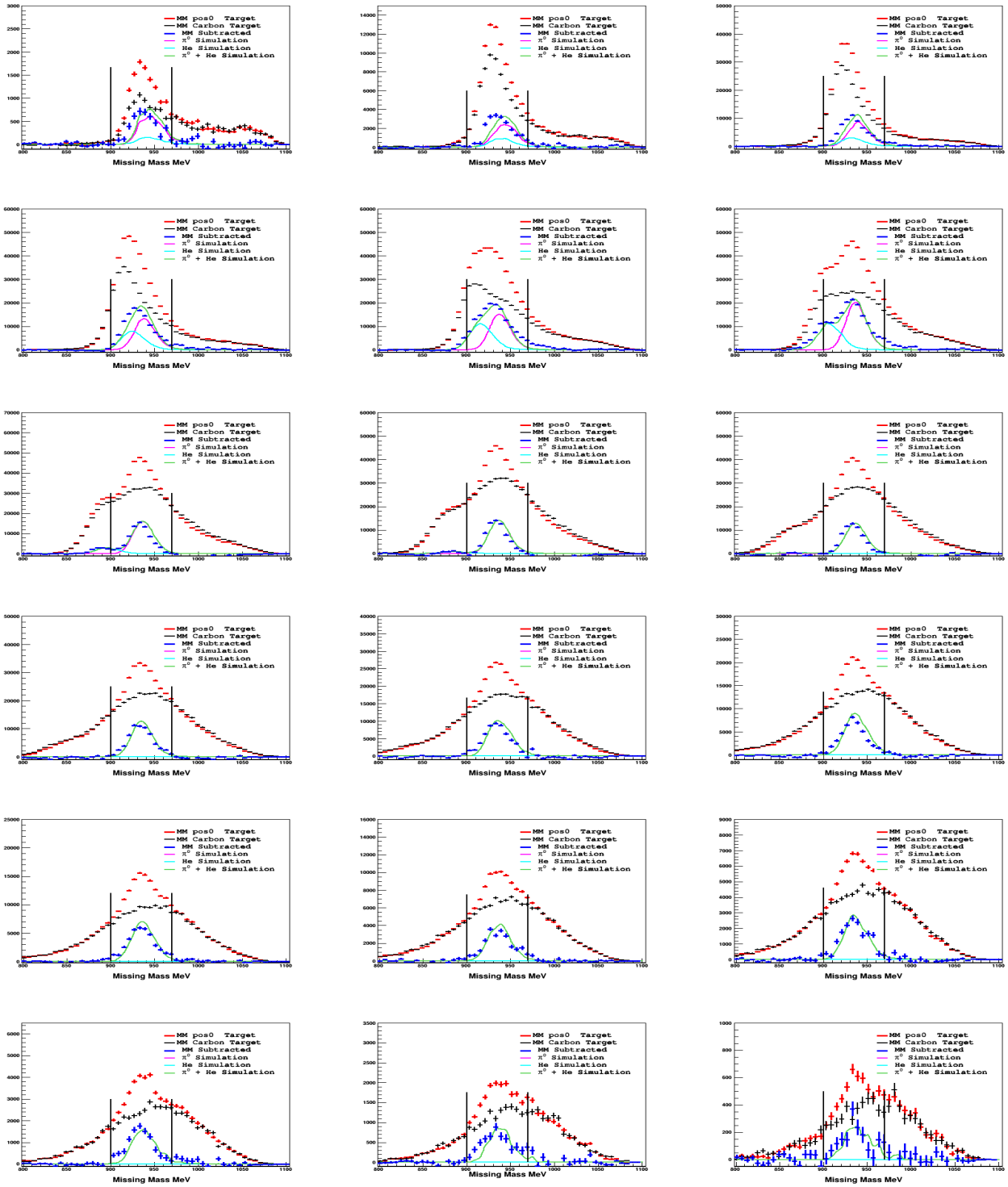

FIG. 49: Missing mass spectrum at $\theta_{\pi^0} = 0-10°, 10-20°, \ldots, 170-180°$ and $E_\gamma = 310-330$ MeV on the π^0 photoproduction channel from the 2015 beamtime. The two vertical lines represent the missing mass integration limit (P0C0).

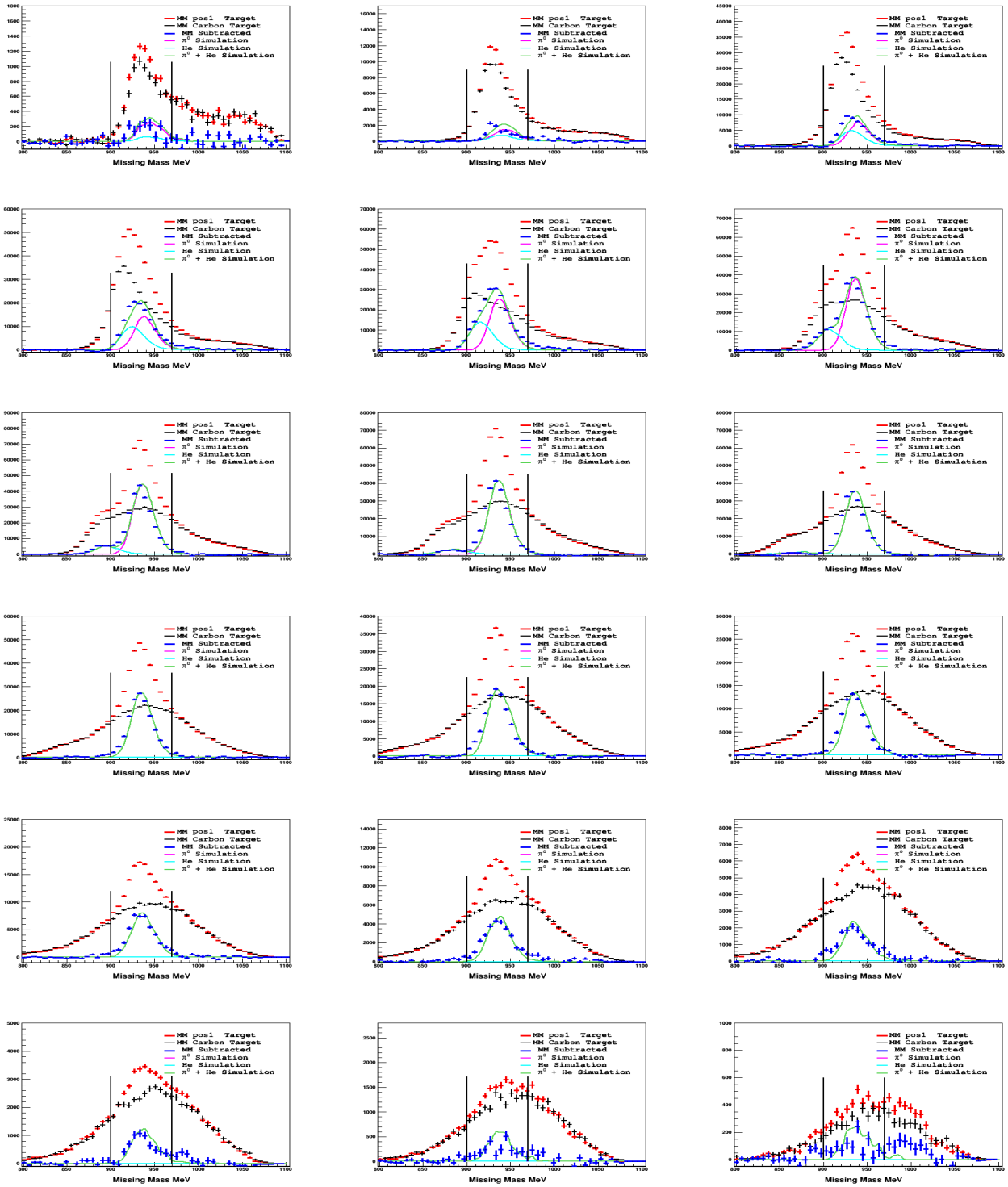

FIG. 50: Missing mass spectrum at $\theta_{\pi^0} = 0-10°, 10-20°, \ldots, 170-180°$ and $E_\gamma = 310-330$ MeV on the π^0 photoproduction channel from the 2015 beamtime. The two vertical lines represent the missing mass integration limit (P1C1).

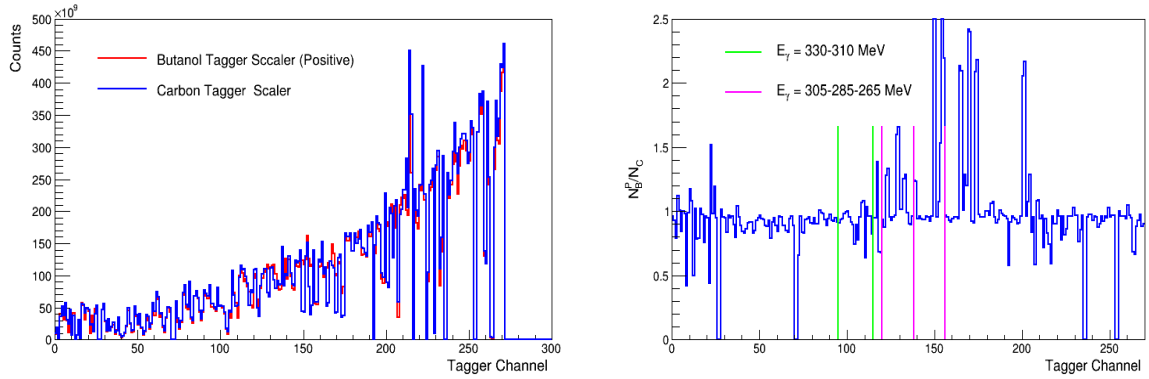

(a) (b)

FIG. 51: (a)Tagger scaler distribution for positively polarized butanol target and carbon target runs. (b) Ratio of butanol tagger scalers (positively polarized target orientation) to carbon tagger scalers. The vertical lines show the tagged energy range of interest corresponding to tagger channels. The fluctuations represent missing tagger channels and the statistical fluctuations.

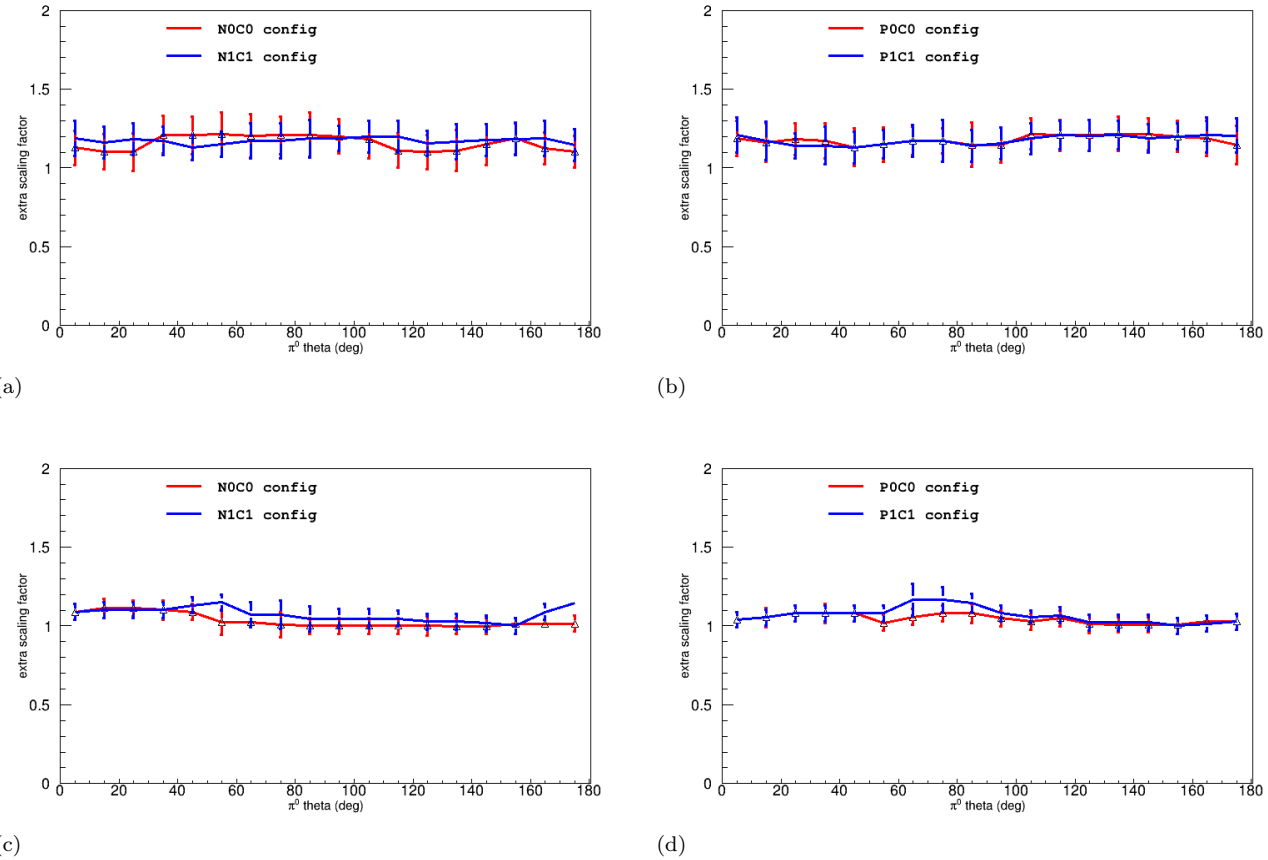

(a) (b)

(c) (d)

FIG. 52: Extra Carbon Scaling Factors. (a) and (b) show an extra carbon scaling factors for negatively and positively polarized target orientations from the 2014 beamtime, (c) and (d) from the 2015 beamtime.